

MICROCOPY RESOLUTION TEST CHART
NATIONAL BUREAU OF STANDARDS-1963-A

A Study of the Diffusion of Tracer Impurities
in the Versator I Tokamak by Spectral Emissions
in the Vacuum Ultraviolet Range

by

plasma

George Patrick Lasche

Courses VIII and XXII

May, 1977

FOR FURTHER TRAN *II*

1

6

A STUDY OF THE DIFFUSION OF TRACER IMPURITIES IN THE VERSATOR I TOKAMAK PLASMA BY SPECTRAL EMISSIONS IN THE VACUUM ULTRAVIOLET RANGE

by

10

GEORGE PATRICK/LASCHE

B.S., United States Military Academy (1969)

9 Master's thesis

SUBMITTED IN PARTIAL FULFILLMENT OF THE REQUIREMENTS FOR THE DEGREE OF

MASTER OF SCIENCE

at the

MASSACHUSETTS INSTITUTE OF TECHNOLOGY

12 65p.

11 May 1977

DDC RECEIVED MAY 16 1978

A

Signature of Author..... Departments of Physics and Nuclear Engineering, May 12, 1977

Certified by..... Thesis Supervisor

Accepted by..... Chairman, Interdepartmental Committee

21 ORIGINAL CONTAINS COLOR PLATES: ALL DDC REPRODUCTIONS WILL BE IN BLACK AND WHITE.

DISTRIBUTION STATEMENT A Approved for public release; Distribution Unlimited

220 000

LD

A Study of the Diffusion of Tracer Impurities in the Versator I
Tokamak Plasma by Spectral Emissions in the Vacuum Ultraviolet Range

by

George Patrick Lasche

Submitted to the Departments of Physics and Nuclear Engineering on
May 12, 1977 in partial fulfillment of the requirements for the
Degree of Master of Science.

ABSTRACT

Diffusion of impurity ions was studied by artificially injecting
neon gas into the Versator I tokamak ($n \sim 2 \times 10^{13} \text{ cm}^{-3}$), $T_e \sim 150 \text{ eV}$,
n sub e about 2x10 to the 13th power/cm.cu. m toroidal magnetic field $\sim 5.5 \text{ kG}$, pulse duration $\sim 7 \text{ msec}$, plasma
sub e about current $\sim 5 \text{ kA}$). Small amounts of neon gas were injected into the
about tokamak by means of a pulsed piezo-electric valve. The absolute
line intensity of vacuum ultraviolet radiation in the range of
400 to 1600 Å, emitted from ions which had been 3 to 7 times ionized,
was observed as a function of time, and along twenty-one chords
across the plasma column. The local density of neon in the plasma in
space and time was determined by use of Abel inversion. From this an
experimental value for the flux rate of this impurity into the plasma
was inferred.

Thesis Supervisor: George Bekefi, Professor of Physics

ACCESSION NO.	
NTIS	White Section <input checked="" type="checkbox"/>
DOS	Buff Section <input type="checkbox"/>
UNANNOUNCED	<input type="checkbox"/>
JUSTIFICATION	
<i>Letter on file</i>	
BY	
DISTRIBUTION / AVAILABILITY CODES	
Dist.	AVAIL. AND/OR SPECIAL
<i>A</i>	

ACKNOWLEDGEMENTS

I would like to express my appreciation to Professor George Bekefi for permitting me to undertake this experiment and for offering much of the information useful in the experiment, and to Professor Larry Lidsky for his useful advice and help.

Special thanks are due to Jim Terry, Kuo In Chen, Roger Richards, and Professor Warren Moos of the Johns Hopkins University, who constructed much of the equipment I used, who gave me advice and instruction in VUV spectroscopy, and who helped me calibrate the monochrometer.

Without Ed Fitzgerald's valuable advice and assistance I could not have constructed the many vacuum and mechanical devices essential to the experiment. Ed Apgar, of the Alcator group, provided me with conductance calibration data and arranged for the use of the Alcator leak valve.

TABLE OF CONTENTS

	<u>Page</u>
ABSTRACT	2
ACKNOWLEDGEMENTS	3
TABLE OF CONTENTS	4
LIST OF FIGURES	6
CHAPTER I INTRODUCTION	
1.1 Background	8
1.2 Purpose and Method	9
CHAPTER II THE EXPERIMENTAL APPARATUS	
2.1 General Description	12
2.2 The Monochrometer	15
2.3 The Detector System	18
2.4 Absolute Calibration of the Monochrometer	18
2.5 The Neutral Impurity Injection Rate	19
CHAPTER III IDENTIFICATION, SELECTION, AND SPATIAL SCAN OF NEON LINES	
3.1 Locating the Radiative Lines of Neon	25
3.2 Confirmation and Identification of Suspected Lines of Neon	28
3.3 Selection of Lines for Spatial Scan	30
3.4 Constraints of Resolution and Reliability	32
3.5 The Spatial Scan	32

TABLE OF CONTENTS (Cont.)

	<u>Page</u>
CHAPTER IV LOCAL EMISSION DENSITIES	
4.1 Locating the Plasma Center	37
4.2 Radial Inversions	37
4.3 Conversions of Radial Inversions to Emissivity	
CHAPTER V APPLICATION OF THE CORONA MODEL	
5.1 Validity of the Coronal Approximation	45
5.2 Rate Equations	45
5.3 Rate Coefficients	46
5.4 Excitation Equilibrium	49
5.5 Relating Emissivity to Ionic Species Density	52
5.6 The Twelfth Species: Ortho-Ne VII	52
5.7 Determination of the Ratio of Ortho-Ne VII to Para-Ne VII	53
5.8 The Absolute Density Distributions of Ne VII and Ne VIII	54
CHAPTER VI DRIFT VELOCITIES AND FUTURE CONSIDERATIONS	
6.1 Approximations to the Corona Equations	56
6.2 Drift Velocities	58
6.3 Future Considerations	59
REFERENCES	62
BIOGRAPHICAL NOTE	64

LIST OF FIGURES

<u>Figure No.</u>		<u>Page</u>
2.1.1	Vacuum Chamber at Elevated Extreme	13
2.1.2	Geometry of Equal Chord Step Heights	14
2.2.1	Vacuum Ultraviolet Monochrometer	16
2.4.1	Quantum Throughput v. Wavelength	20
2.5.1	Pressure v. Time in Alcator Ballast	22
3.1.1	Spectrum Histogram	27
3.2.1	Brightness v. Time of Successive Neon Radiative Lines	29
3.2.2	Integrated Signal v. Time at Neon Radiative Lines With and Without Neon	31
3.5.1	Comparison of Two Plasma Currents and Brightness Signals With and Without Neon	34
3.5.2	Experimental Data Taken from Oscillographs	36
4.1.1	Total RMS Error for Assumed Centers	38
4.2.1	Emissivity in Time and Radius of Ne IV through Ne VIII	41
4.3.1	Radiation from a Volume Element	43
4.3.2	Relation of Collimating Aperture and Entrance Slit to Plasma	43
4.3.3	Approximation of Dimensions of Plasma Viewed by Entrance Slit	43
5.3.1	Excitation Rate Coefficients of Ne VII	47
5.3.2	Excitation Rate Coefficients of Ne VIII	48

LIST OF FIGURES (Cont.)

<u>Figure No.</u>		<u>Page</u>
5.3.3	Ionization Rate Coefficients for Neon	50
5.3.4	Recombination Rate Coefficients for Neon	51
5.8.1	Absolute Densities of Ne VII and Ne VIII	55
6.1.1	Ratio of Ionization to Recombination Rate Coefficients for Neon	57
6.2.1	Drift Velocities of Ne VIII	60

CHAPTER I INTRODUCTION

1.1 Background

One of the problems which affect the prospects of tokamaks as fusion reactors is the question of the behavior of impurities in a tokamak plasma. If they tend to reside in the hot core of the plasma, they may cause so much power loss by brehmsstrahlung and line radiation that thermonuclear ignition may never be reached. The problem is especially serious since heavy impurities will be highly ionized in thermonuclear plasmas and brehmsstrahlung radiation is proportional to the square of the ionic charge. At thermonuclear temperatures, line radiation losses can be greater than the brehmsstrahlung radiation losses. Moreover, energy confinement time and plasma channel radius are affected by the effective charge density distribution.

The most direct way to study such impurities is to observe them spectroscopically. If they still possess bound electrons, these electrons may be excited by collisions or absorption, and, upon deexcitation, emit photons of wavelengths characteristic to the impurity ion. The best quantitative conclusions about impurity density can be drawn if resonance transitions are observed, since they are usually the most likely and in a low density plasma most excitations can be assumed to have originated from the ground state. The wavelengths of resonance transitions are typically

short (100 to 1000 Angstroms), and are therefore transmitted through matter and reflected by matter with poor efficiency. For this reason, they are best observed by placing a spectrometer in vacuum with the plasma.

Recent work using vacuum ultraviolet spectroscopy has been done by the TFR Group,^{1,2} who studied the diffusion of impurities naturally occurring in the TFR tokamak, such as oxygen, iron, and molybdenum. The rate of introduction of these impurities during the discharge was not known. In order to study diffusion of impurities whose source function is known, Cohen, Cecci, and Marmor³ irradiated aluminized glass by laser light in the ATC tokamak. Aluminum ions at radii greater than 8 cm were observed using vacuum ultraviolet spectroscopy and found in radial distributions in agreement with the predictions of a computer model using neoclassical diffusion theory.⁴

It has been difficult to draw good conclusions about the impurity transport to the central core of tokamak plasmas, since at the high temperatures at the core of most tokamak plasmas impurity ions are either fully stripped of electrons so that they have no characteristic deexcitation photon emissions or are so highly ionized that the resonance emissions are of very short wavelength and difficult to measure with good spatial resolution.

1.2 Purpose and Method

It is the purpose of the experiment herein described to study

the diffusion of impurities throughout a tokamak plasma by artificially injecting an impurity known not to be otherwise present and observing its evolution in space and time spectroscopically. Neon was chosen as the "tracer" impurity since at the relatively cool Versator I temperatures (approximately 150 eV) it does not become fully stripped of electrons, and provides a distribution of ionic species whose resonance wavelengths are well into the range of good instrument detection and resolution. In addition, the transition wavelengths, oscillator strengths, subshell binding energies, and transition probabilities of neon have been well studied and measured.^{6,7}

In order to obtain spatial resolution, the brightness as a function of time was measured along chords across the plasma column displaced from the axis by 1 cm increments. If the impurity distributions are assumed radially symmetric with respect to the center of the plasma column, the radial distribution of the emissivity of each ionic species observed can be deduced by use of Abel's inversion formula.⁸ From knowledge of the electron temperature and density distributions, the rate of excitation of ground state ions can be calculated, making possible a conclusion about the actual density distribution of each species of the impurity.

Finally, the mass flow of the impurity can be estimated by comparing the local time rate of change in density to that predicted

by ionization and recombination of neighboring ($Z \pm 1$) species.

CHAPTER II THE EXPERIMENTAL APPARATUS

2.1 General Description

The Versator I tokamak has a main field of about 5 kG, a toroidal plasma current of 5.5 kA, electron density of $2 \times 10^{13}/\text{cm}^3$, electron temperature of 150 eV, a minor radius of 14 cm with no limiter, a major radius of 54 cm, and a pulse duration of 7 mS. The largest port is the pumping port, which provides the greatest field of view of the plasma column.

A vacuum ultraviolet monochrometer was mounted inside a magnetically shielded vacuum chamber, which was connected to the pumping port extension by means of a flexible vacuum connection. The chamber was mounted on a frame which could be raised and lowered, pivoting about the center of the flexible connection. Figure 2.1.1 shows the chamber raised to its extreme. Measurement with an alignment laser showed that the maximum radius which could be observed was ± 9 cm. The chamber could be raised to +13 cm and -10 cm, so that the entire field of observation lay within its limits.

For a radially symmetric plasma, chords converging through a point can be made equivalent to parallel chords at different heights, as can be seen from Figure 2.1.2. It was desirable that the perpendicular distance from the poloidal axis to the chord be a multiple of increments of the same step height for simplification

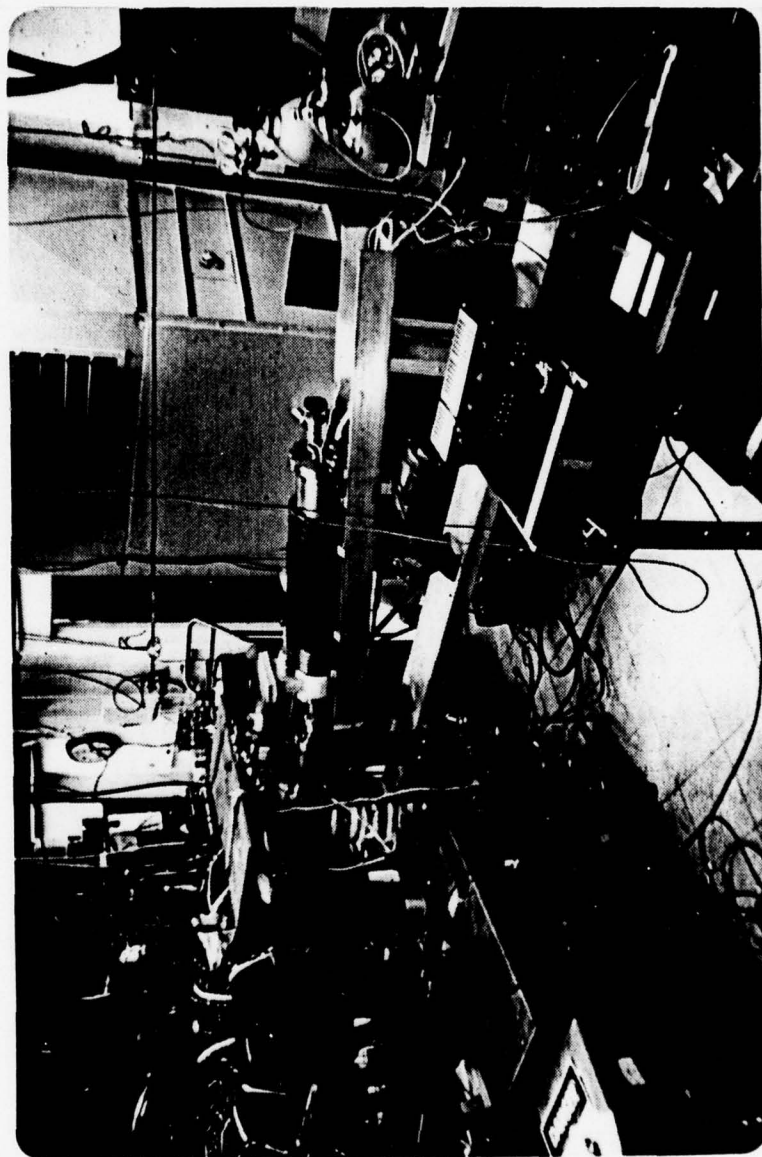


Figure 2.1.1.1 Vacuum Chamber at Elevated Extreme

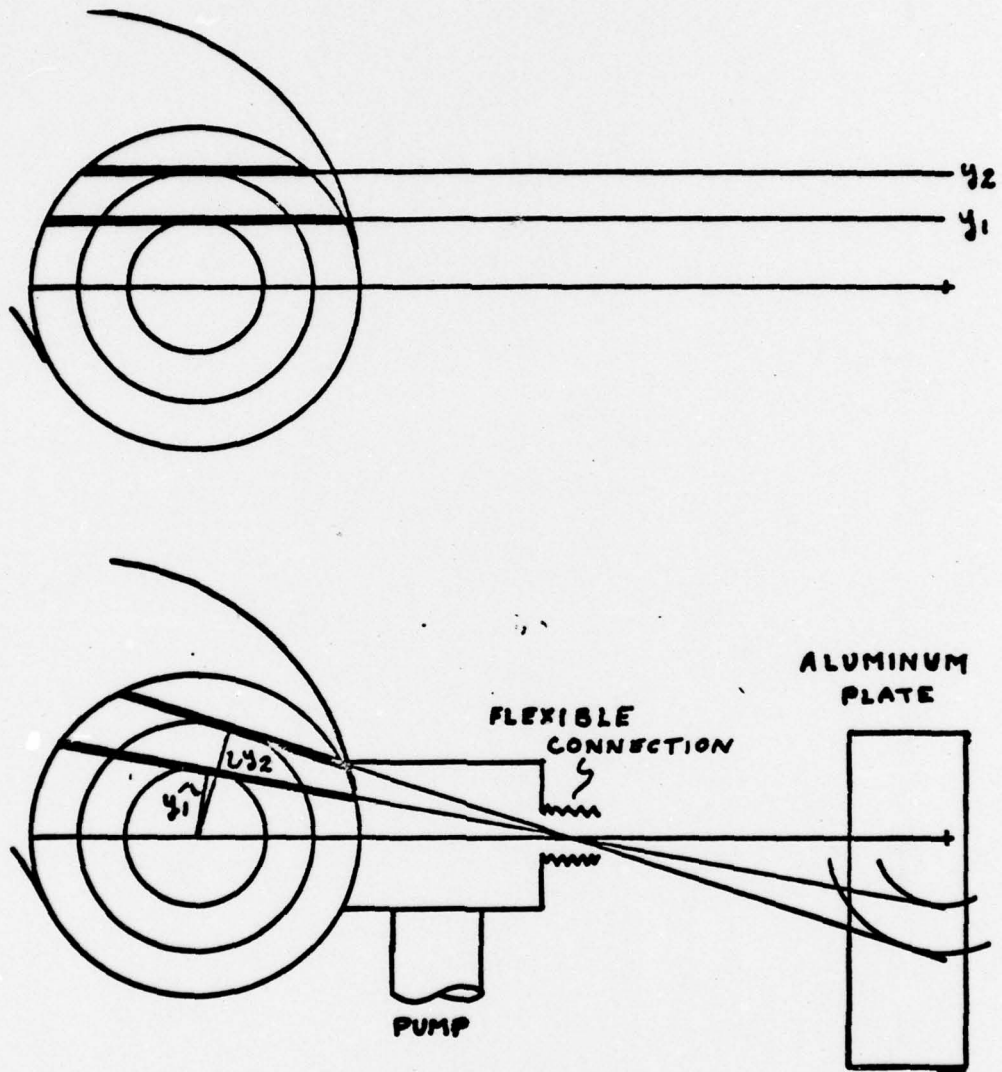


Figure 2.1.2 Geometry of Equal Chord Step Heights

of analysis. Since the best spatial resolution was of the order of 1 cm, that distance was chosen for the increment step height. In order to provide a direct measurement of the chord height from the axis, the projection of all heights and the poloidal axis through the pivot axis was inscribed on a plate of aluminum at an equal distance away from the poloidal axis as indicated in Figure 2.1.2. The frame supporting the vacuum chamber was then aligned with the inscribed mark corresponding to the desired off-axis height. This very simple method eliminated the need for many computations and indirect measurements, and thereby eliminated the possibility of associated errors.

At a point 90 degrees from the pumping port in the toroidal direction was mounted a piezo-electric gas leak valve. It was connected to a supply of research grade neon, and pulsed open by applying 100 volts for 1 millisecond to the piezo-electric crystal, causing it to deform and leak neon gas into the tokamak at the desired time. A controlled pressure system was constructed so that the neon supply pressure to the valve could be adjusted in order to better control the amount of neon leaked.

2.2 The Monochrometer

The vacuum ultraviolet monochrometer (shown in Figure 2.2.1) was on loan from the Johns Hopkins University, and is similar to those designed by W. G. Fastie for sounding rocket research. Its light weight, compact size, and remote control design made it

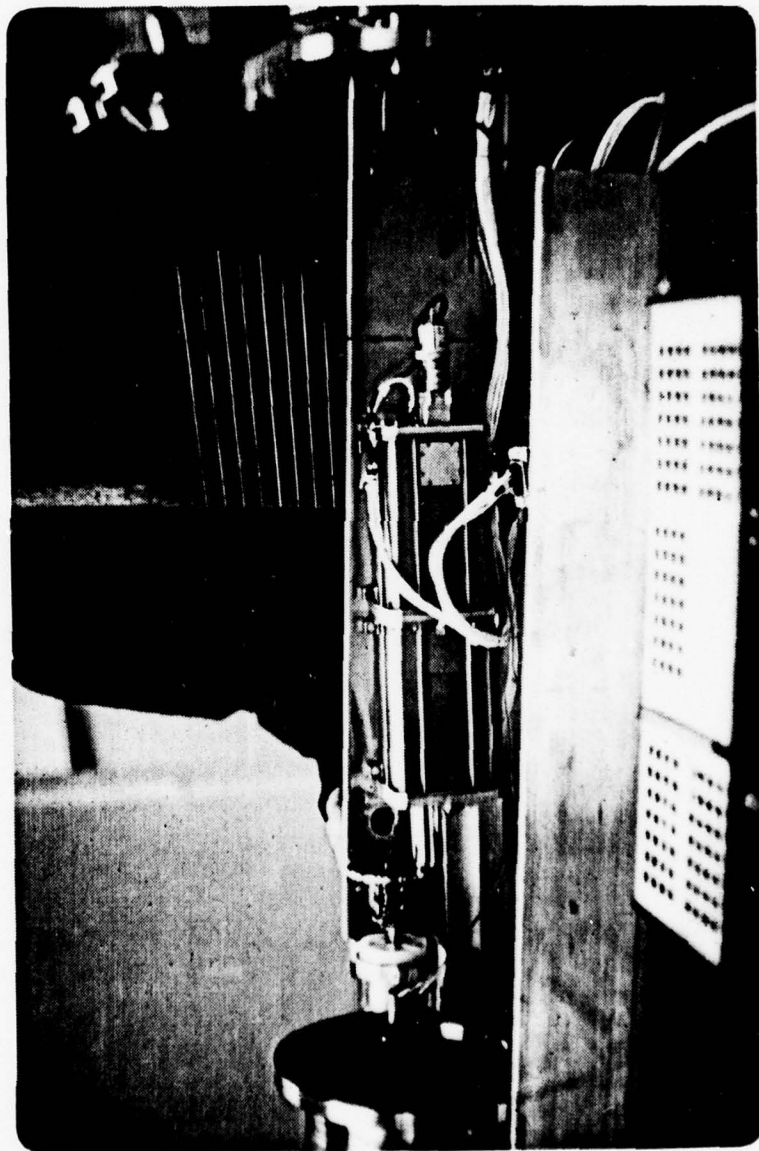


Figure 2.2.1 Vacuum Ultraviolet Monochrometer

particularly suitable for the experiment. It employed a holographic grating with 3600 lines/mm and a dispersion of $12 \text{ \AA}/\text{mm}$. It was a normal incidence monochromator, using fixed entrance (.083x1 mm) and exit (.25x5 mm) slits, and a focal length of 22.5 cm. Since the grating rotated, but did not translate, it was not always in focus on the Rowland circle.⁹ To allow for this imperfect focus and to allow for broadening of the emission lines, the large (.25 mm) exit slit was used, resulting in a spectral resolution of 3 \AA . This was adequate for the purpose, however, since line separation was of this order and it was desirable to pass the entire spectrum of the broadened emission lines, since the higher flux permitted greater spatial and time resolution by allowing more narrowly collimated fields of observation and shorter time windows. Moreover, more accurate determination of the density of emitters is possible if the entire broadened line is observed, since errors due to calculations of what portion of the line is seen are not present. The height of 5 mm at the exit slit ensured that dispersion due to astigmatism did not preclude reflected photons from reaching the detector.

The grating was mounted on a frame which could be rotated by digital control, with each angular step referenced by a "lambda count" ranging from 0 to 1000. This corresponded roughly to wavelengths of 800 to 1600 \AA in first order, and 400 to 800 \AA in second order.

For collimation, a disk with holes was placed 5.65 cm from the

entrance slit toward the plasma, permitting the selection by remote control of apertures of several diameters, or the selection of LiF or CaF₂ cutoff filters. Collimating apertures of diameter .0559 cm for strong lines and of .157 cm for weaker lines were used throughout most of the experiment, providing focal numbers of 108 and 38.15 respectively.

2.3 The Detector System

The detector was a windowless photomultiplier employing a copper iodide detector surface for better sensitivity at longer wavelengths. For each pulse from the detector, one count was registered on a double hexadecimal counting system. When the system was "strobed" with a trigger pulse, it delivered an output signal linearly proportional to the number of counts (with a maximum of ten volts), and reset the counter to zero. The number of counts registered between strobe pulses was therefore the output signal in volts times $16^2/10$. Digitization in this manner eliminated errors due to variance in amplitude of the photomultiplier signal.

2.4 Absolute Calibration of the Monochrometer

The monochrometer and detector were calibrated absolutely in intensity before and after the data was taken, to insure the characteristics had not changed during the experiment as a result of the photon flux on the grating and detector head surface. Calibration was done at the Johns Hopkins University using the

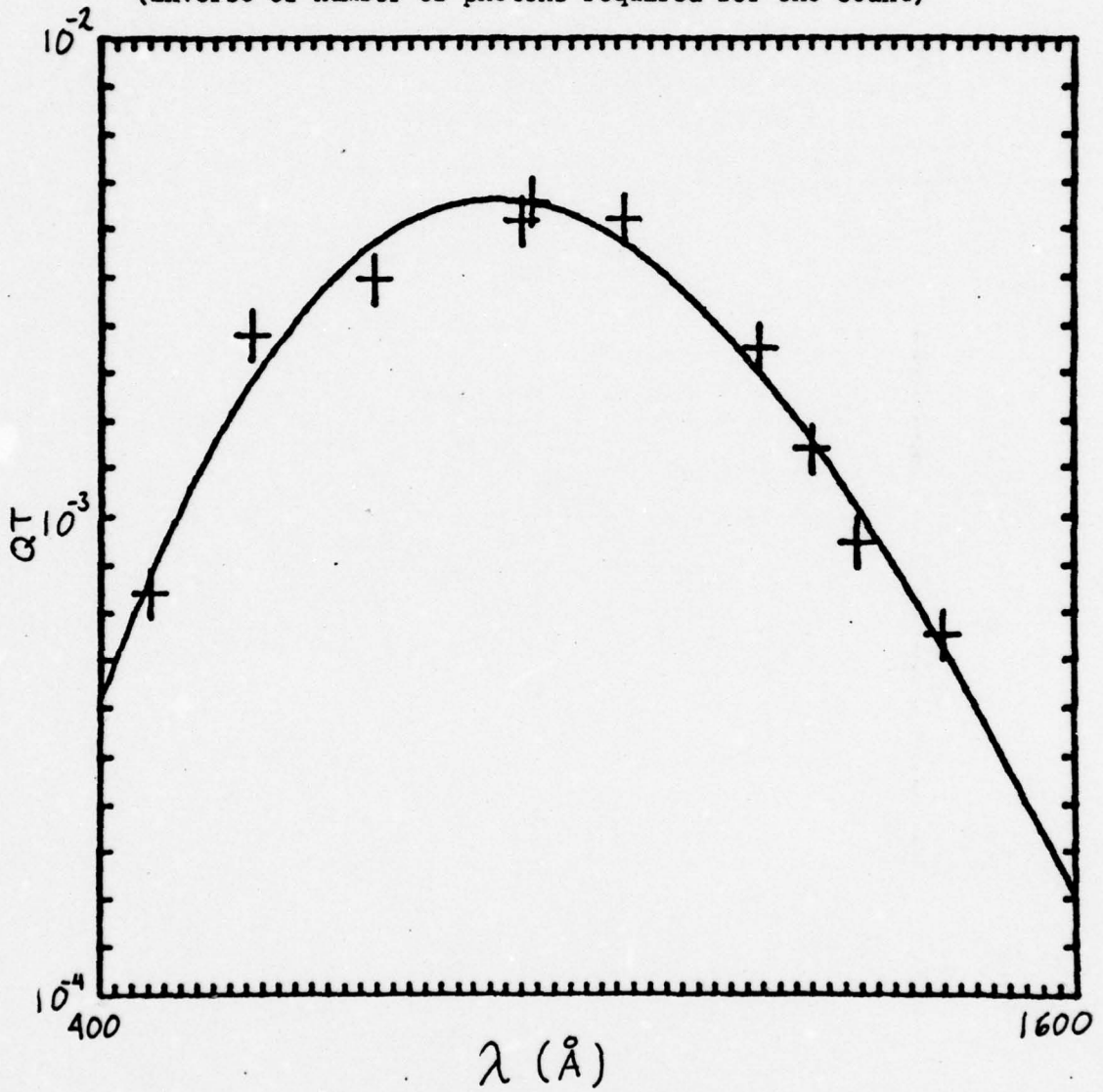
CTE (for 1200 - 1600 Å) and EUV (for 400 - 1200 Å) facilities located there. Light from a gas discharge was allowed to fall incident on the facility grating, which was at first rotated so that a narrow beam of reflected light would be directed entirely on the surface of a photodiode which had just previously been calibrated at the nearby National Bureau of Standards. The magnitude of the signal from the photodiode gave a measure of the absolute intensity of the beam. The facility grating was then rotated through a small angle so that the beam then fell entirely on the instrument grating (both the entrance and exit slits had been removed in order not to block some portion of the beam), and the signal from the instrument detector head was recorded. This gave a measure of the combined efficiency of the grating reflection and of the detector response, designated the quantum throughput. The He line at 584 Å; the Ne lines at 460 and 735 Å; the Ar lines at 920 and 1048 Å; and the H lines at 1216, 1280, 1336, and 1440 Å were measured; yielding the QT as a function of wavelength, shown in Figure 2.4.1, together with a best fit polynomial for interpolation. The characteristics of the response were found not to have varied outside the limits of probable error of the calibration procedure (about 10%), during the course of the experiment.

2.5 The Neutral Impurity Injection Rate

The valve used for the experiment was the Veeco model PV-10. Experimentation with this valve showed that its response character-

QUANTUM THROUGHPUT

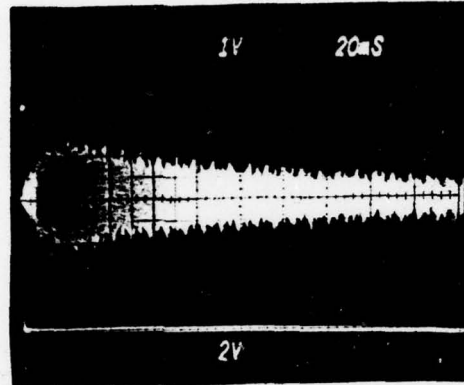
(Inverse of number of photons required for one count)



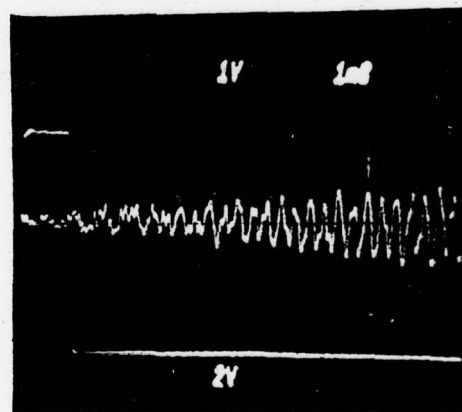
istics to applied voltage pulses (square waves) sharply increased above a threshold voltage (about 84 volts), varied nonlinearly with the pulse duration, and also depended critically on the time period between pulse applications. In order to introduce as little neon as possible but maintain good reproducibility, it was found that at an interval between pulses of 30 seconds, a pulse of 100 volts applied for 1 millisecond was well suited, with the neon supply pressure lowered to 200 Torr.

A valve of the same model has been mounted on the Alcator tokamak, for the injection of hydrogen during discharges. The Alcator valve is equipped with a MKS type 315 BHS-1SP fast high accuracy capacitance manometer, mounted on a ballast volume between the valve and the tokamak. Since a fast guage of this type was not available to the Versator I experiment, the neutral impurity injection rate through the valve was measured using the Alcator equipment with the assumption that the response characteristics of the two valves are approximately the same. To minimize any other differences, the same pulse generator used for the Versator experiment was used at Alcator, with the same pulse height, duration, and time between pulses.

The results are shown in Figure 2.5.1. The pressure envelope increases in amplitude at an approximately constant rate from 0 to .9 volts during the first 10 milliseconds, which is the time interval of interest. The guage output was adjusted to 1 volt per



(20 mS/Division)



(1 mS/Division)

Figure 2.5.1 Pressure v. Time in Alcatator Ballast

micron. Therefore

$$\frac{dP}{dt}_{\text{ballast}} \approx \frac{.9 \text{ microns}}{10 \text{ mS}} = .09 \text{ Torr/sec} \quad (2.5.1)$$

The ballast volume was measured to be 1.03 liters and the conductance to the Alcator tokamak to be 110 liters/sec, taken from the calibration data of pressure versus flow rate made at Alcator. Since the flow into Alcator was

$$Q_{\text{Alcator}} = G \times P(t) = 9.9t \text{ Torr-lit/sec} \quad (2.5.2)$$

and the rate of accumulation in the ballast volume was

$$V \frac{dP}{dt} = 1.03 \times .09 = .0927 \text{ Torr-lit/sec} \quad (2.5.3)$$

the gas flow out of the PV-10 valve was the sum of the flow into Alcator and the accumulation in the ballast volume

$$Q_{\text{valve}} = Q_{\text{Alcator}} + V \frac{dP}{dt} = 9.9t + .0927 \text{ Torr-lit/sec.} \quad (2.5.4)$$

The conductance of the valve was

$$G(t) = \frac{Q(t)}{P} = .013t + .000122 \text{ lit/sec.} \quad (2.5.5)$$

At low pressure, the ideal gas model is appropriate. Since neon is a monatomic gas, one Torr-liter at room temperature (293° K) corresponds to 3.29×10^{19} atoms.

Since the valve at Versator was mounted on the tokamak surface, the neutral impurity injection rate is taken to be equal to the conductance of the valve times the pressure differ-

ence of 200 Torr

$$Q_{\text{Versator}} = G \times P = 8.58 \times 10^{19} t + 8.03 \times 10^{17} \text{ atoms/sec (2.5.6)}$$

The total number of atoms injected is the time integral of flow

$$N(t) = 4.29 \times 10^{13} t^2 + 8.03 \times 10^{14} t \text{ atoms (t in mS). (2.5.7)}$$

CHAPTER III IDENTIFICATION, SELECTION, AND SCAN OF NEON LINES

3.1 Locating the Radiative Lines of Neon

Since the monochrometer had not been calibrated in wavelength, it became necessary to deduce which radiative lines of the several neon ionic species corresponded to which digital wavelength reference number (lambda count). To do this, the approximate lambda count of every allowed transition of every species of neon in first, second, and third order was estimated by interpolation between those values used during the absolute calibration of the monochrometer (Sec. 2.4). Portions of the spectrum including all these transitions were then selected for examination.

Then, stepping the lambda counter in increments of one, the tokamak was discharged at each lambda count and the time-integrated signal noted. The plasma current profile of each discharge was checked to insure reproducibility, and those discharges which were disruptive were rejected. In order to obtain a quantitative basis for comparison, a simple integrator was built using a capacitor, diode, and resistor and connected to a digital voltmeter to represent total signal received during the discharge at that lambda count. The signal time profile was also noted on the oscilloscope, with attention paid to the time a peak occurred and the ratio of the peak to the plateau of the signal profile. The entire process was then repeated with about 1% neon mixed in the hydrogen

feed line, which was about as much as possible without producing any noticeable changes in the plasma current profile. The results of the scan without neon are shown in the bottom of Figure 3.1.1, and those with neon directly above. The simple difference is shown above the first two.

It can be noted that most of the major lines which appeared in the "without neon" spectrum reappeared when the simple difference of the two signals was taken. This is partly the result of the digital wavelength control, operating in quantum increments, failing to set the grating at the exact same angle when the same lambda count was selected. The result is slight variation in the portion of a line spectrum covered, and consequent variance in the signal heights when the same lambda count was redialed. Later, in taking data for spatial and temporal inversions, this problem was solved by redialing the same lambda count several times until a peak was reached, and then doing the entire spatial scan without redialing. The top histogram of Figure 3.1.1 shows the difference of "with" and "without" neon enhanced to account for the wavelength variation in lambda count: the "without" spectrum was shifted down one lambda count and up one lambda count, and half that sum added to the unadjusted "without" spectrum. This total was then subtracted from the "with" spectrum, with resulting elimination of many of the impurity lines with relatively little effect on the neon lines (notice the O V line of 776 Å). The

SPECTRUM HISTOGRAM

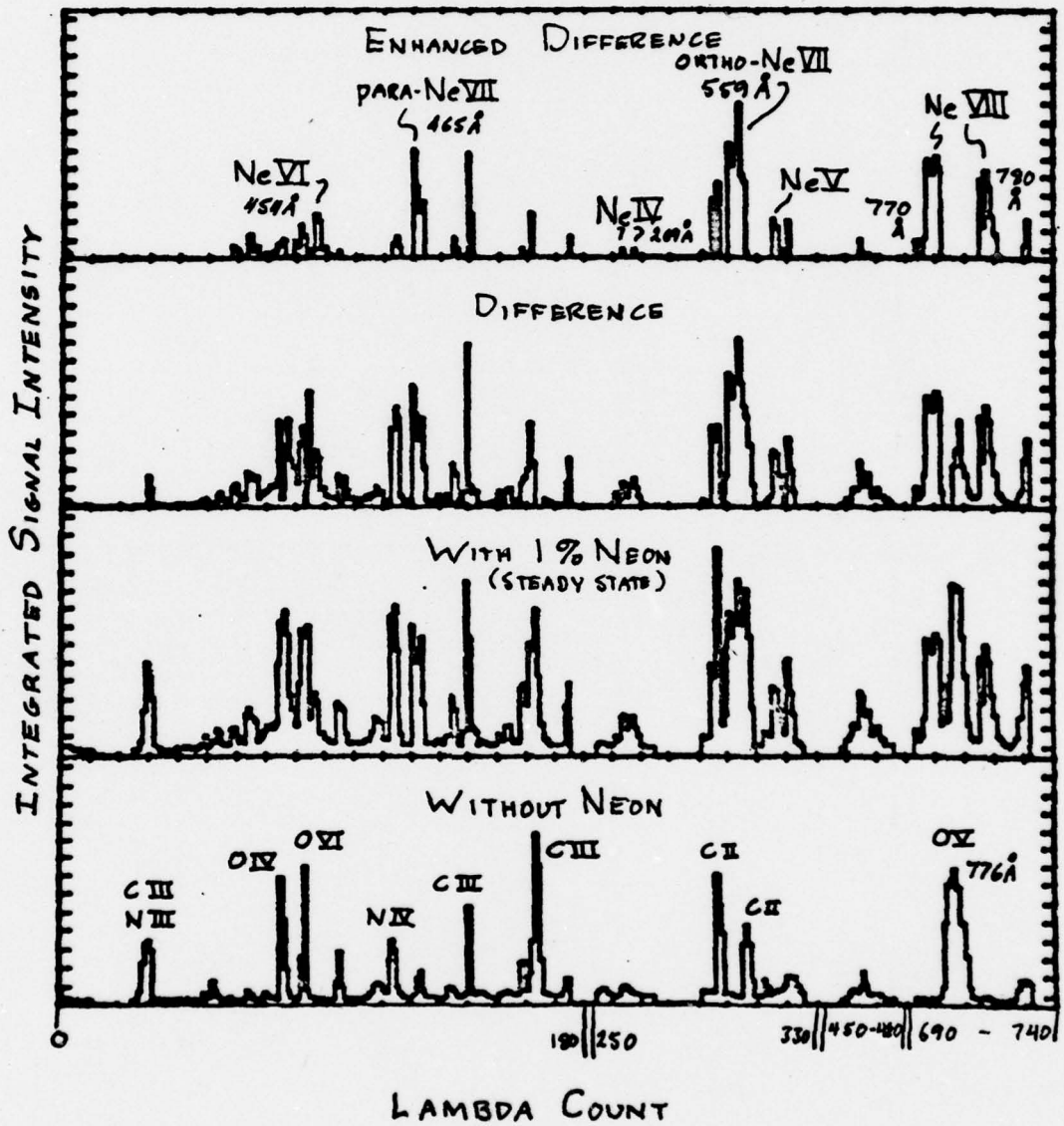


Figure 3.1.1

remaining lines, if strong, were then investigated with strong suspicion of being true neon lines.

3.2 Confirmation and Identification of Suspected Lines of Neon

If they were in fact neon lines, then they were appearing in second order. Since the instrument resolution was 3\AA , and 3\AA in second order equals twice the angle of rotation of the grating as in first order, the width of the instrument broadening of the line gave an indication of the order. For those lines greater in wavelength than about 600\AA , their failure to appear after interposition of the LiF cutoff filter confirmed they were not of first order, since the LiF cutoff was about 1200\AA . Furthermore, reference to the sensitivity calibration (see Sec. 2.4) shows that efficiency is very poor for wavelengths less than 400\AA , eliminating the need to consider third order possibilities.

After the neon lines were tentatively identified, the time of peak and the peak-to-plateau ratio was checked. The lesser ionized species should have peaked earlier in the discharge, and have had a higher peak-to-plateau ratio since they are quickly ionized into more highly ionized species, and the more highly ionized species should have appeared successively in time as the electron temperature increased. This was indeed the case when the brightness-time traces (shown in Figure 3.2.1) of the different suspected species of neon were compared. To provide further confirmation of the wavelength of suspected neon lines, nearby

BRIGHTNESS V. TIME PROFILES OF
SUCCESSIVE NEON RADIATIVE LINES
(STEADY STATE MIXTURE OF NEON IN H₂,
ORDINATE NOT NORMALIZED.)

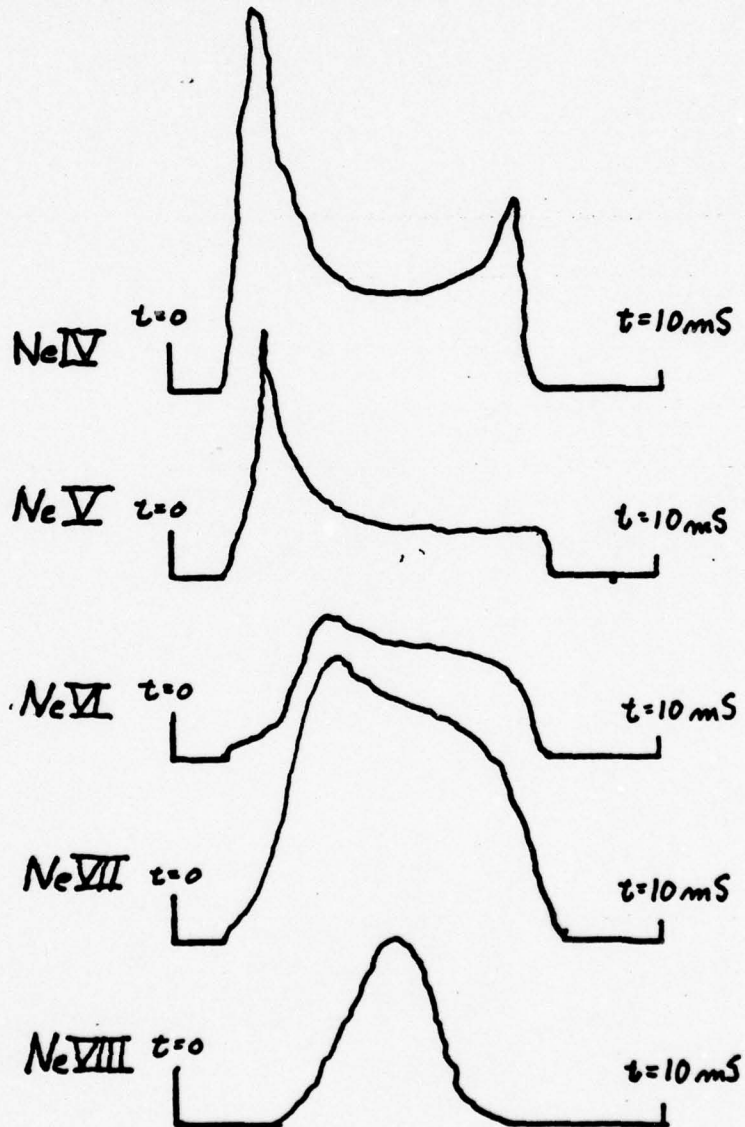


Figure 3.2.1

oxygen, nitrogen, carbon, and hydrogen provided convenient "landmarks", as well as indications of the natural impurity content. Sometimes, however, they obscured neon lines of interest. Those lines which could be identified are labeled in Figure 3.1.1.

As a final check, the valve controlling the flow of neon was alternately closed and opened while the lambda count remained set on the peak of a suspected line. The resulting signals from several such trials are shown in Figure 3.2.2. Also shown are the results of the same experiment performed at a nearby lambda count not suspected to be a wavelength of neon as a control to insure the increased signals were not due solely to the addition of impurity.

3.3 Selection of Lines for Spatial Scan

The lines selected for the spatial scans were those 1) with bright signals, 2) distant from lines of naturally present impurities, 3) distant from other neon lines, and 4) of resonance transitions if possible. "Distant" means instrument broadening width (in second order, about 3 lambda counts). It was possible to observe fairly weak lines of Ne IV, Ne V, and Ne VI; and relatively bright lines of Ne VII and Ne VIII (in spectroscopic notation Ne I is neutral neon, so that these species were respectively three, four, five, six, and seven times ionized). Interestingly, the brightest line of Ne VII was not a resonance transition, a phenomenon which will be discussed later on.

INTEGRATED SIGNAL V. TIME AT NEON
RADIATIVE LINES

WITH (UNSHADED) AND WITHOUT (SHADED) NEON

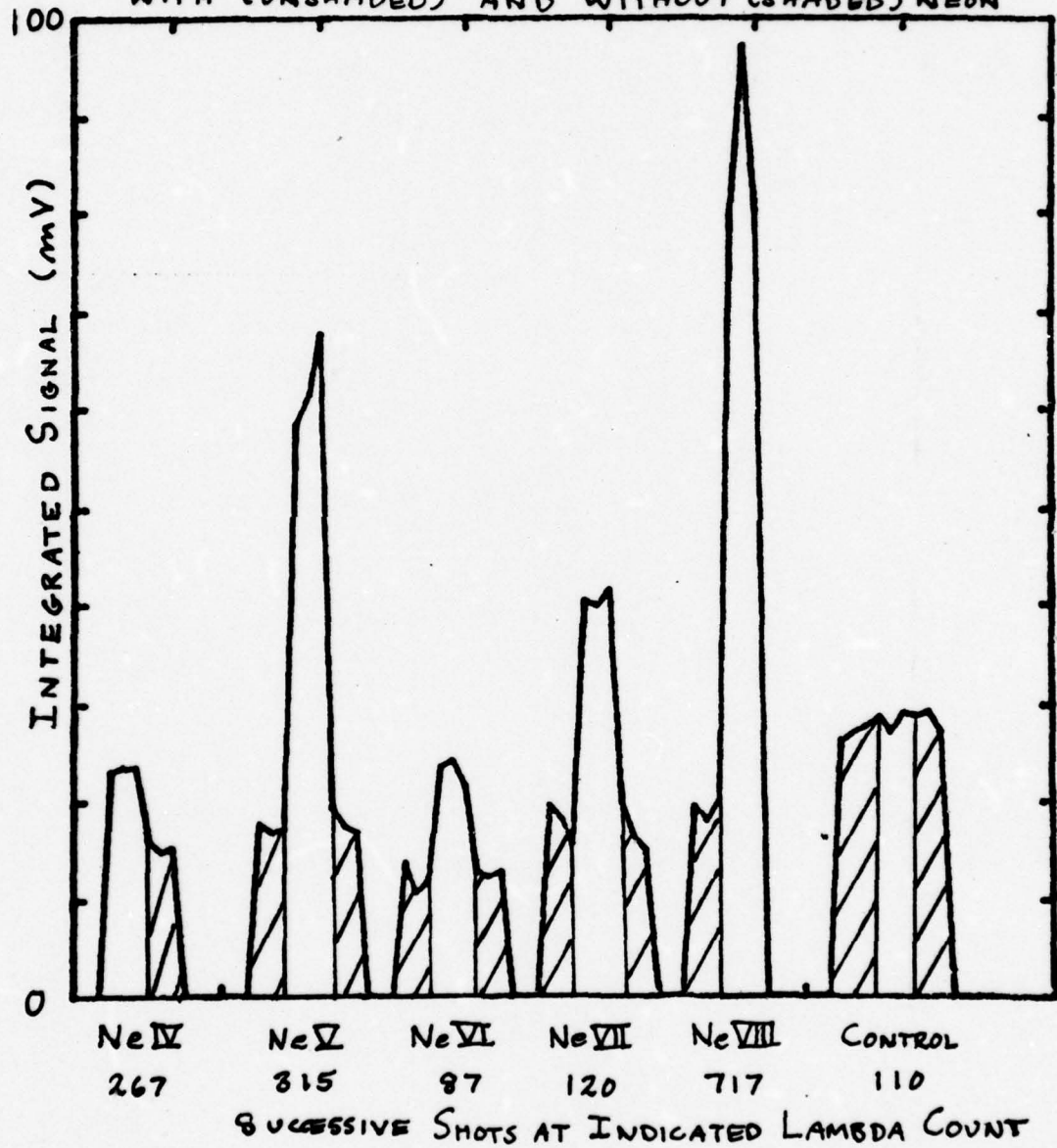


Figure 3.2.2

3.4 Constraints of Resolution and Reliability

In order to obtain a statistically reliable result, at least 40 counts between strobe pulses were considered necessary to overcome Poisson statistical variations. As an upper constraint, both the 256 maximum count capacity of the digital system and the saturation limit of the photomultiplier had to be considered. In addition, the time between strobe pulses had to be short compared to the scale time of the change of signal in order to obtain good time resolution during the plasma discharge. On the other hand, the time between strobe pulses had to be long enough to obtain the statistical requirement of 40 counts while using collimating apertures small enough to obtain good spatial resolution. (Increasing the source intensity of the neon lines was not practical beyond a certain limit since adding too much neon to the plasma would change the plasma characteristics too severely to accomplish the objective of the experiment). With these factors in mind, a time between strobe pulses of .1 mS was used for the stronger signals, and of .33 mS for the weaker ones.

3.5 The Spatial Scan

The spatial scan was conducted across twenty-one chords spaced off the poloidal axis in increments of one centimeter for each of the species Ne IV through Ne VIII. The plasma current profile was checked after each discharge and those with no breakdown, disruptive plasmas, or otherwise irreproducible discharges were

rejected. Similarity in plasma currents was taken to indicate sufficient reproducibility in plasma from which each of the brightness-time profiles were taken for each of the chord heights for each of the ionic species. The entire process was then repeated injecting no neon. The signal thus obtained represented the unwanted continuum radiation and the line radiation from impurities other than neon, so that the difference was a measure of the signal due solely to the line radiation of neon. To insure the characteristics were not slowly changing in time, the signal on axis was taken at the beginning and end of each scan, and compared for reproducibility.

Each signal was recorded by photographing the oscilloscope trace made by the photomultiplier signal and the plasma current profile. Shown in Figure 3.5.1 is an oscilloscope trace taken of the Ne VII line at lambda count 300, directly through the geometrical poloidal axis of the tokamak. Superimposed on the trace is another trace taken without injecting neon. One can observe that there is very little difference in the plasma current profiles (superimposed at the bottom), while the photomultiplier output signals (at the top) differ significantly later in the discharge. The square wave at the beginning of the top trace is the voltage applied to the neon injection valve (for the first shot only). The shorter of the two currents corresponds to that in which neon was injected, indicating the plasma resistivity is increased

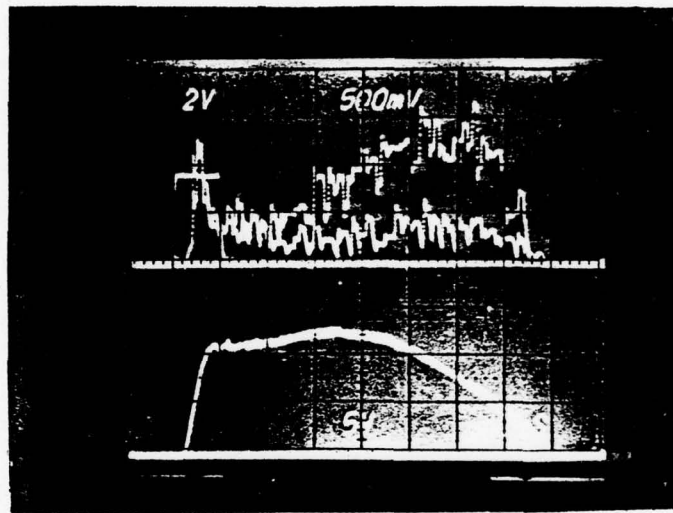


Figure 3.5.1 Comparison of Two Plasma Currents
and Brightness Signals With and Without Neon

somewhat by the injected impurity. Each horizontal division represents one millisecond. In this case there were ten strobe pulses per millisecond.

Once the complete set of photographs had been taken, the traces were projected for enlargement, and the signal differences at one, two, three, four, and five milliseconds measured and recorded for each photograph. The results are displayed in Figure 3.5.2. A visual inspection indicates several things of interest: the lower ionization states appear earlier; the higher ionization states are concentrated toward the middle of the plasma; the lower ionization states appear to be hollow shells since the brightness profiles do not increase toward the center; the plasma column appears to be shifted off the geometrical poloidal axis toward the right (down, in the tokamak); and, most importantly, the distributions appear to be radially symmetric. Without this last observation, the Abel inversion technique to determine radial density would not be valid.

EXPERIMENTAL DATA TAKEN
FROM OSCILLOGRAPHS

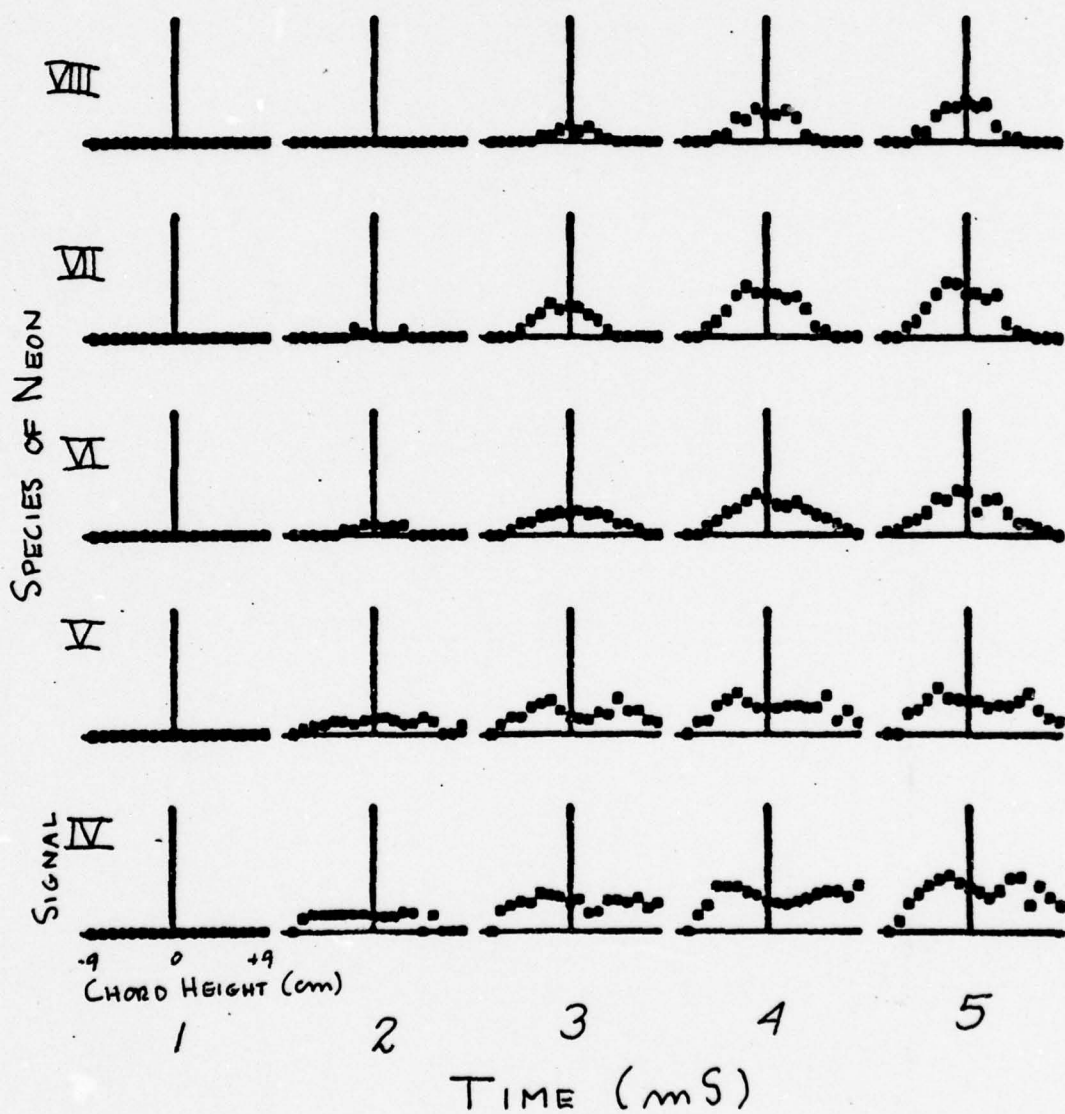


Figure 3.5.2

CHAPTER IV LOCAL EMISSION DENSITIES

4.1 Locating the Plasma Center

In order to obtain the distribution in space (two dimensions, assuming symmetry toroidally around the tokamak) given a one-dimensional spatial array, an assumption must be made with respect to one of the two dimensions to be obtained. If it is assumed the distributions are radially symmetric about some plasma poloidal axis, the inversions can be done, but first that plasma center must be determined.

The method used was first to numerically best fit fourth order even polynomials (for symmetry about the origin) to each set of data, using a spectrum of assumed centers. The RMS error from each data point of the resulting curves was totaled for each of the assumed centers. The results are shown in Figure 4.1.1. In this way, the center of the plasma was determined to be two centimeters below the geometrical axis. This can be explained by magnetic field errors or by the collimating line being slightly off parallel with the mount for the vacuum chamber. The lower three and upper two points were then discarded since they were possibly false due to partial or full eclipsing of the plasma column by physical obstructions.

4.2 Radial Inversions

With the assumption of radial symmetry, the Abel inversion

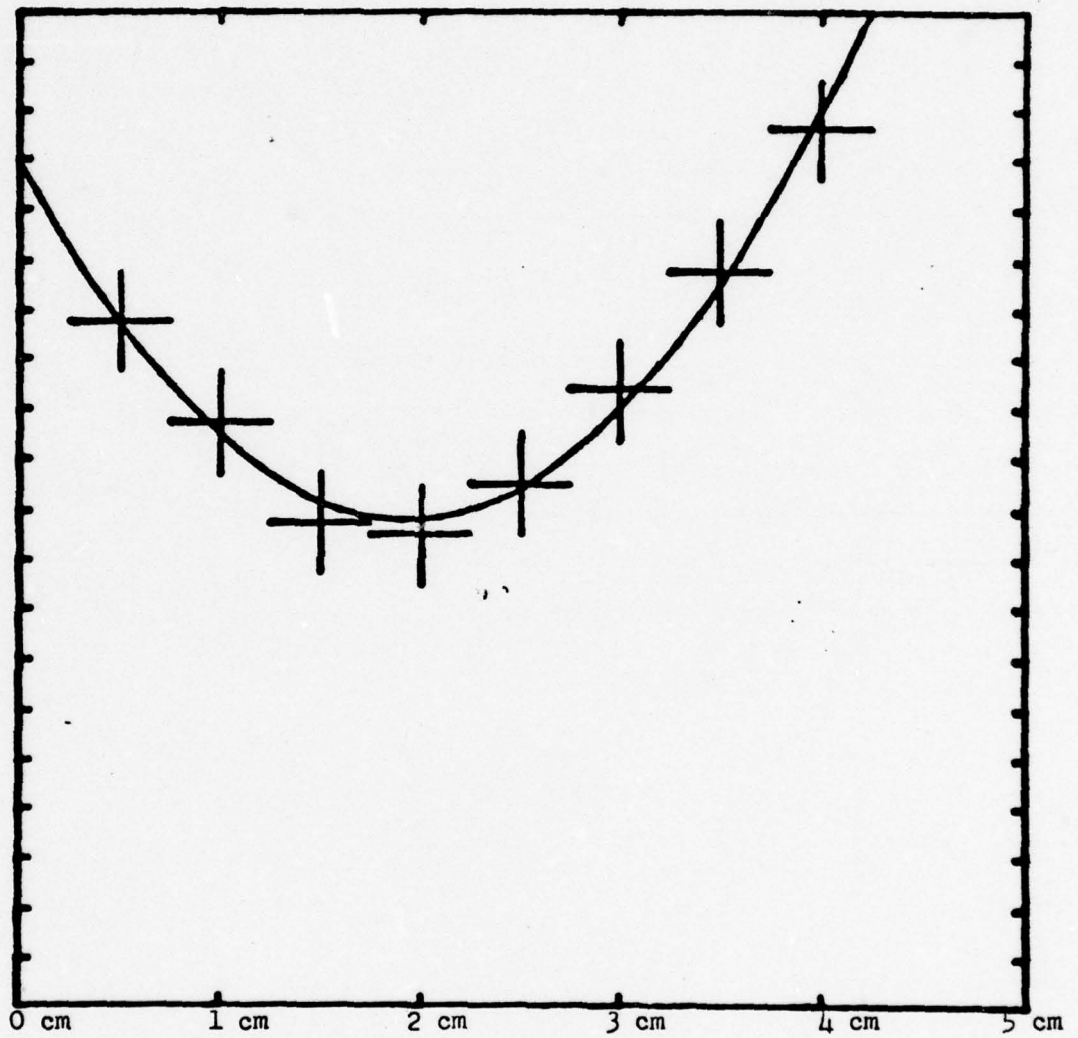


Figure 4.1.1 Total RMS Error for Assumed Centers

formula⁸ can be used to determine the radial density of emitters, given the brightness as a function of chords displaced from the axis of symmetry. To equate the brightness to the integrated emission density function along the chord length, one must further assume that reabsorption of photons emitted in the plasma is negligible (optical thinness), that reflections from the far wall are negligible, and that the height of the plasma within view of the detector is small compared to the radial scale distance over which the emission changes, (for this reason the monochrometer was oriented as shown in Figure 2.2.1, with the longest dimension of the entrance slit parallel to the poloidal axis).

The effective absorption coefficient is given by⁸

$$k' = \frac{\pi e^2}{2mc} f_{mn} N_n (1 - e^{-h\nu/kT}) \quad (4.2.1)$$

where f_{mn} is the absorption oscillator strength and N_n the density of the lower states of the line. Taking the largest oscillator strength of the lines observed (.57 for Ne VII), and the largest density ($1 \times 10^{11} \text{ cm}^{-3}$) the value of the coefficient is $2.27 \times 10^{-3} / \text{cm}$. Across the observed plasma radius of 10 cm, the maximum signal attenuation due to absorption is $1 - e^{-k'r}$ or 1.1%. Since this value was obtained using a most unfavorable case, it is safe to assume that negligible loss of signal was due to absorption.

By comparing the photomultiplier efficiency with the quantum

throughput of the monochrometer, it can be concluded that no more than 5% of the photons at the observed wavelengths which strike the grating are reflected. Since the reflection efficiency of the tokamak wall directly back to the entrance slit must be much less, the assumption that reflected photons from the tokamak wall are negligible is valid.

In order to obtain sufficient signal, the lines of Ne VII and Ne VIII were observed with an effective height of view of the plasma of 1.6 cm, and those of Ne VI, Ne V, and Ne IV with 4.5 cm. Comparison with the scale length of density change in radius (Sec. 5.7) shows that the assumption of narrow height of view is valid only for Ne VII and Ne VIII, and that the inversions of the other lines should be taken for their qualitative value only, keeping in mind that the true shapes must have sharper changes, since such a wide view height would have the effect of smoothing out and averaging any changes in signal.

The Abel inversions were done using a technique of local smoothing of the brightness derivatives¹⁰ prior to integration, in order to most effectively allow for experimental error. The results are shown in Figure 4.2.1. Considering the relatively wide view heights used for the lower three ionic species, the true peaks of the lower three states probably occur about 2 cm further out in radius.

EMISSIONIVITY

(NOT NORMALIZED)

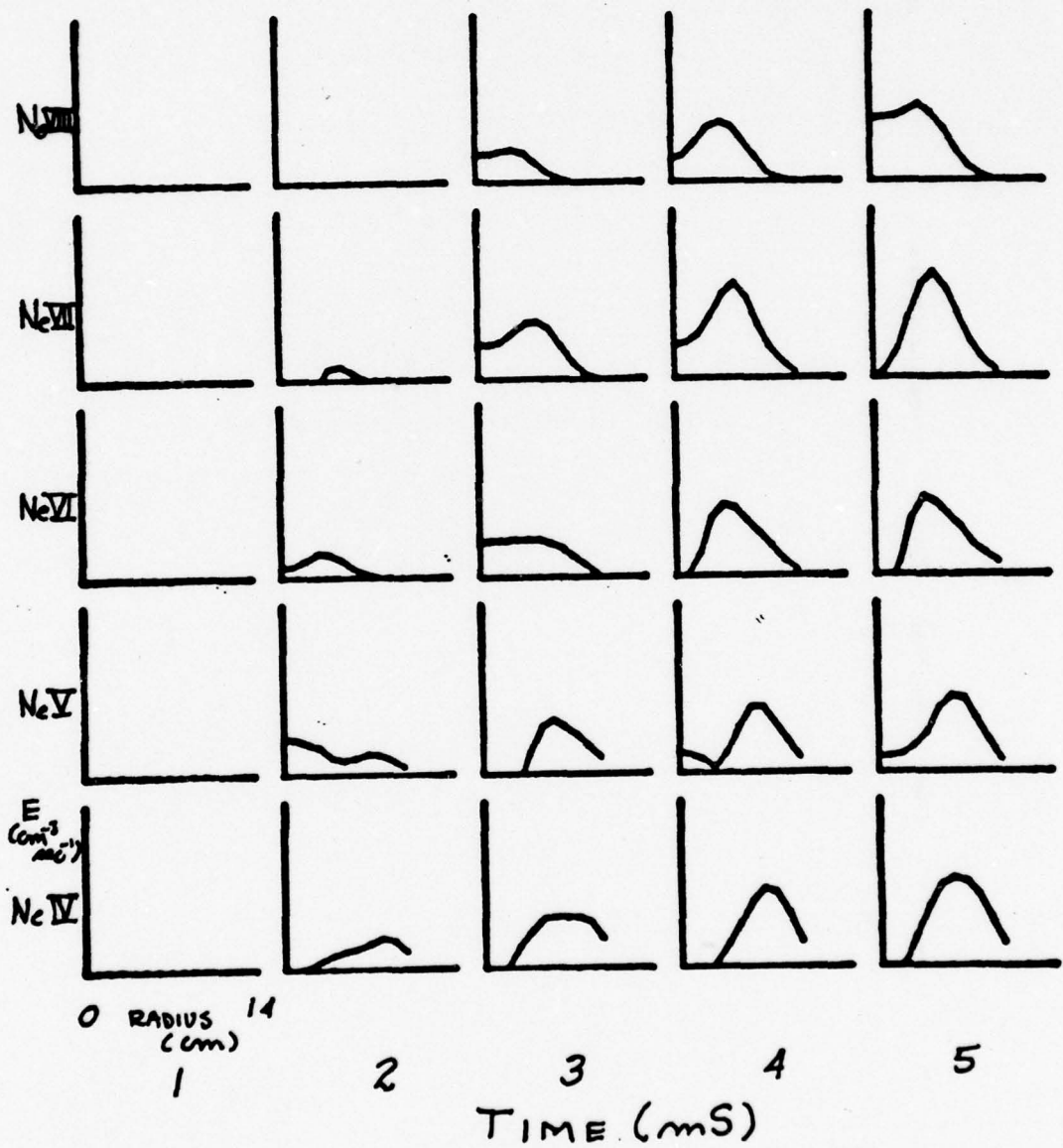


Figure 4.2.1

4.3 Conversion of Radial Inversions to Emissivity

Dividing the count rate (the product of the signal, strobe frequency, and the constant 25.6 counts/volt) by the quantum throughput yields the photon rate through the entrance slit (number of photons of wavelength λ per second). The photon rate through the entrance slit is related to the emissivity (number of photons of wavelength λ per cubic centimeter per second) in the plasma in the following way.

For a differential volume element of plasma as in Figure 4.3.1, radiating isotropically at E photons/cm³sec at the wavelength of interest, a sphere of radius $R+l$ receives $1/4\pi(R+l)^2$ of the radiation per unit area. At a distance R away, the collimating aperture, of diameter d , is located. At a distance l behind the aperture is the instrument entrance slit of height h , small compared to all other dimensions.

Since l is small compared to R , the rays passing the aperture are nearly parallel, and the portion of the entrance slit illuminated by dV is approximately of width d . The fraction of emitted radiation passing both aperture and slit is the illuminated area of the slit divided by the area of the sphere of radius $R+l$. Therefore the number of photons passing through the slit per second from the entire plasma is the integral of $Edh/4\pi(R+l)^2$ over the volume of plasma which can be viewed through the entrance slit. Since the

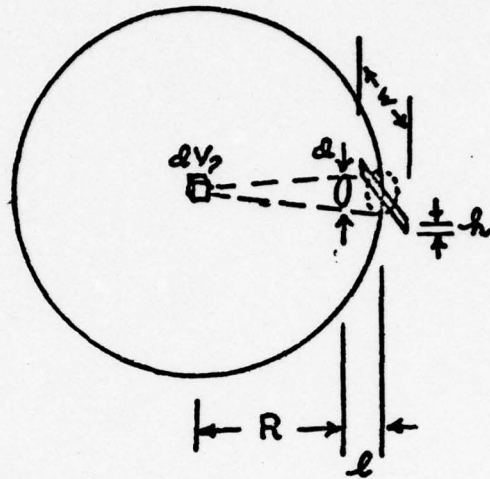


Figure 4.3.1 Radiation from a Volume Element

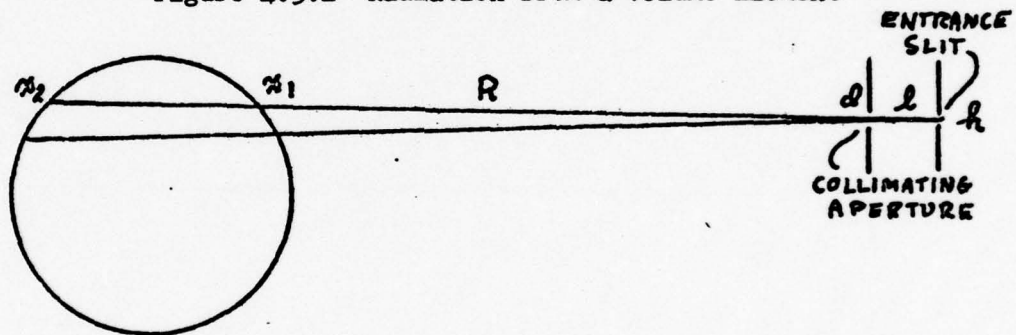


Figure 4.3.2 Relation of Collimating Aperture and Entrance Slit to Plasma

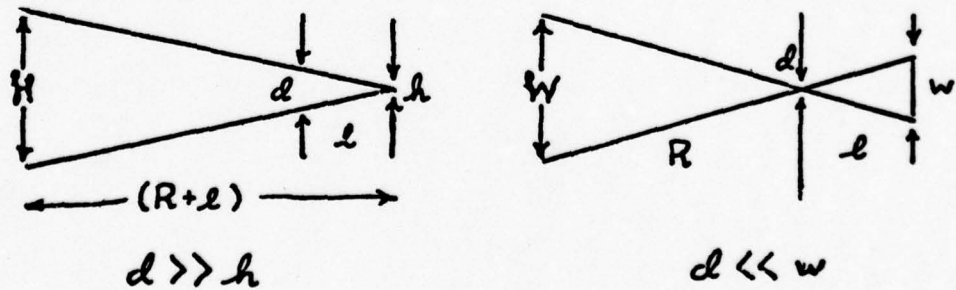


Figure 4.3.3 Approximation of Dimensions of Plasma Viewed by Entrance Slit

radius of the plasma is much smaller than $(R+l)$, the cross-sectional area of the plasma viewed by the entrance slit does not change significantly along the line of sight (see Figure 4.3.2), and if the height of the area is small compared to the scale length of change in $E(r)$, the area can be brought out of the integral, leaving:

$$\text{photons/sec passing slit} = \text{Area seen by slit} \times \frac{dh}{4\pi(R+l)^2} \int_{x_1}^{x_2} E(r) dx \quad (4.3.1)$$

Now the area of the plasma seen by the slit can be approximated in the following manner. Noting that d is much greater than h (see Figure 4.3.3), the height H of the area seen is $(d/l)(R+l)$. Noting the slit width w is much greater than d , the width W of the area seen is Rw/l . Thus, the total area of plasma seen by the entrance slit is approximately $(d/l)(R+l)(Rw/l)$.

Substituting this value into Equation 4.3.1 and using (in centimeters) $d=.05588$, $l=5.6515$, $h=.00833$, $R=154.94$, and $w=.1$, the photon rate passing the entrance slit becomes the product of the constant 6.254×10^{-9} and the emissivity integrated along the length of the chord. The emissivity is therefore obtained by dividing the results of the inversions of Figure 4.2.1 by this constant after converting the detector signal to the photon rate, and represents the product of the excited state density and the decay probability (in sec^{-1}) of the deexcitation transition of the wavelength observed.

CHAPTER V APPLICATION OF THE CORONA MODEL

5.1 Validity of the Coronal Approximation

By comparing the Saha equilibrium and the corona equilibrium equations, one can solve for an electron density above which, at a given electron temperature and ionizational potential, the Saha model is more applicable and below which the corona model applies.¹¹ For the Versator I tokamak this transition value for electron density is about $2.2 \times 10^{19} / \text{cm}^3$, well above the electron densities of 2×10^{13} actually present. In the corona model only two-body collisions need be considered, of which ion-ion collisions are much less frequent than electron-ion collisions.

5.2 Rate Equations

Since neutral neon has ten electrons, there are eleven species of neon ions, ranging from neutral to fully stripped. The probability that an ion of species "j" will be ionized by electron collision to the next higher species "j+1" is the product of a temperature dependent rate coefficient " $S_{j,j+1}$ " and the local electron density. This product, times the local density of ions of species "j" yields the average number of ions of species "j+1" produced each second by ionization of ions of species "j". Similarly, the number of ions of species "j+1" which combine with a free electron to form an ion of species "j" is represented by the product of the two densities

and another temperature dependent rate coefficient " $\alpha_{j+1,j}$ ". A third rate coefficient " $Q_j^{i,k}$ " represents the probability that an ion of species "j" in energy state "i" will be excited to energy state "k" by a collision with a free electron.

The rate of change of the densities of the ionic species then can be written as a set of eleven coupled differential equations:

$$\frac{dn_j}{dt} = \frac{\partial n_j}{\partial t} + \nabla(n_j v_j) \\ = (S_{j-1,j} n_{j-1} - S_{j,j+1} n_j - \alpha_{j,j-1} n_j + \alpha_{j+1,j} n_{j+1}) n_e \\ \text{for } j = 1 \text{ to } 11 \quad (5.2.1)$$

The rate of change of the density of excited state "k" of species "j" can be expressed

$$\frac{dn_j^k}{dt} = n_e \sum_i Q_j^{i,k} n_j^i - n_j^k \sum_i A_j^{k,i} + \sum_i A_j^{i,k} n_j^i \quad (5.2.2)$$

where the $A_j^{k,l}$ are the transition probabilities for the various decay transitions from the excited states.

5.3 Rate Coefficients

Excitation rate coefficients (in cm^3/sec) for all allowed transitions of Ne VII and Ne VIII up to the 3 level are shown in Figures 5.3.1 and 5.3.2 respectively. They were calculated using the formulas of Van Regemorter,¹² who applied correction terms to theoretical predictions to better match experimental values. Ionization rate coefficients using the formulas of Lotz,^{13,14} which account for differences in subshell binding energies, are

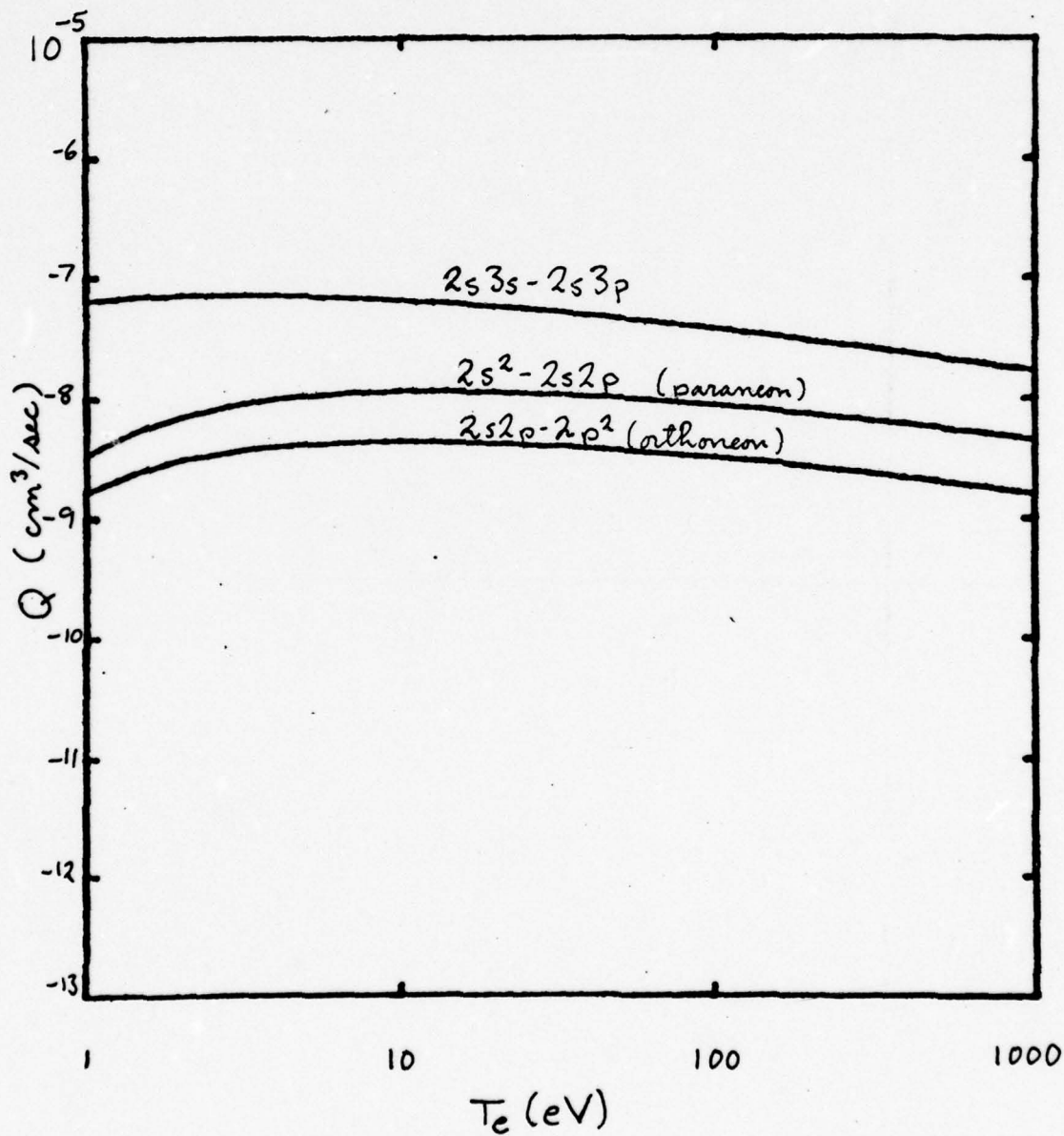
EXCITATION RATE COEFFICIENTS.
NE VII

Figure 5.3.1

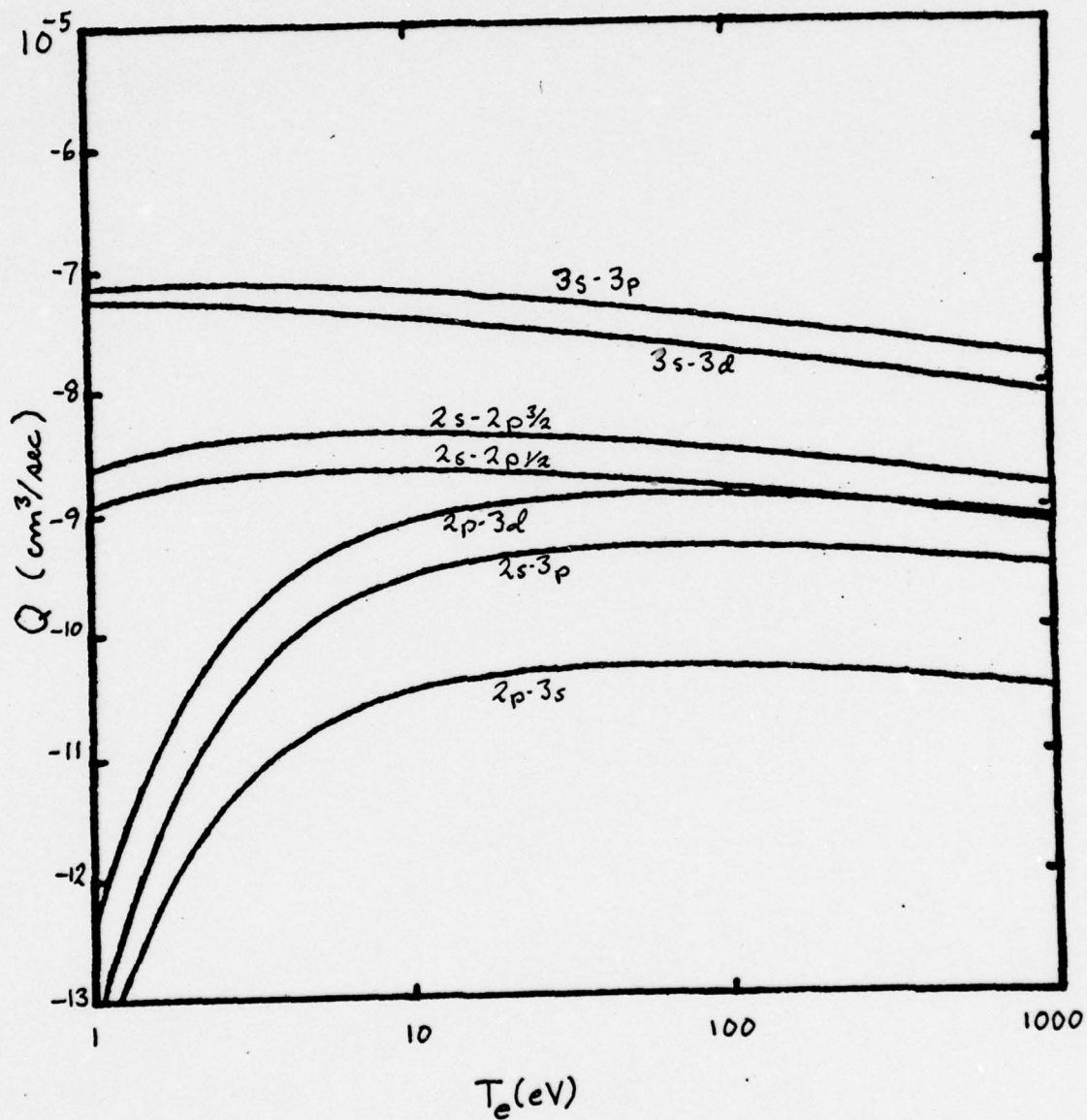
EXCITATION RATE COEFFICIENTS
Ne VII

Figure 5.3.2

shown in Figure 5.3.3. Recombination rate coefficients using Hinno's formula¹⁵ are shown in Figure 5.3.4. Fortunately, in the electron temperature range encountered in Versator I (100 to 150 eV) the ionization and excitation rates vary little with temperature, so that small errors in the electron temperature distribution have negligible effect on the rate equations. Furthermore, the recombination rates for the less highly ionized species in these temperature regimes are typically much lower than the ionization rates for the next lower species, so that recombination rates can be neglected as long as the densities of next higher species are comparable in magnitude.

5.4 Excitation Equilibrium

The plasma has been shown to be optically thin, so that it may be assumed that all excitations take place by electron collisions. Ionization, recombination, and excitation times are calculated by $1/Sn_e$, $1/\alpha n_e$, and $1/Qn_e$ respectively. Deexcitation times are given by¹⁶ $1/\frac{1}{2} A^{k,i}$. Since the times between ionizations and recombinations are large compared to deexcitation times, the left hand term in Equation 5.2.2 can be set to zero since excitation equilibrium is soon reached. Furthermore, since time between excitations is much larger than any of the deexcitation times, in a relatively short time all excited states (with one notable exception) reach the ground state, so that the number density of ground state ions is much

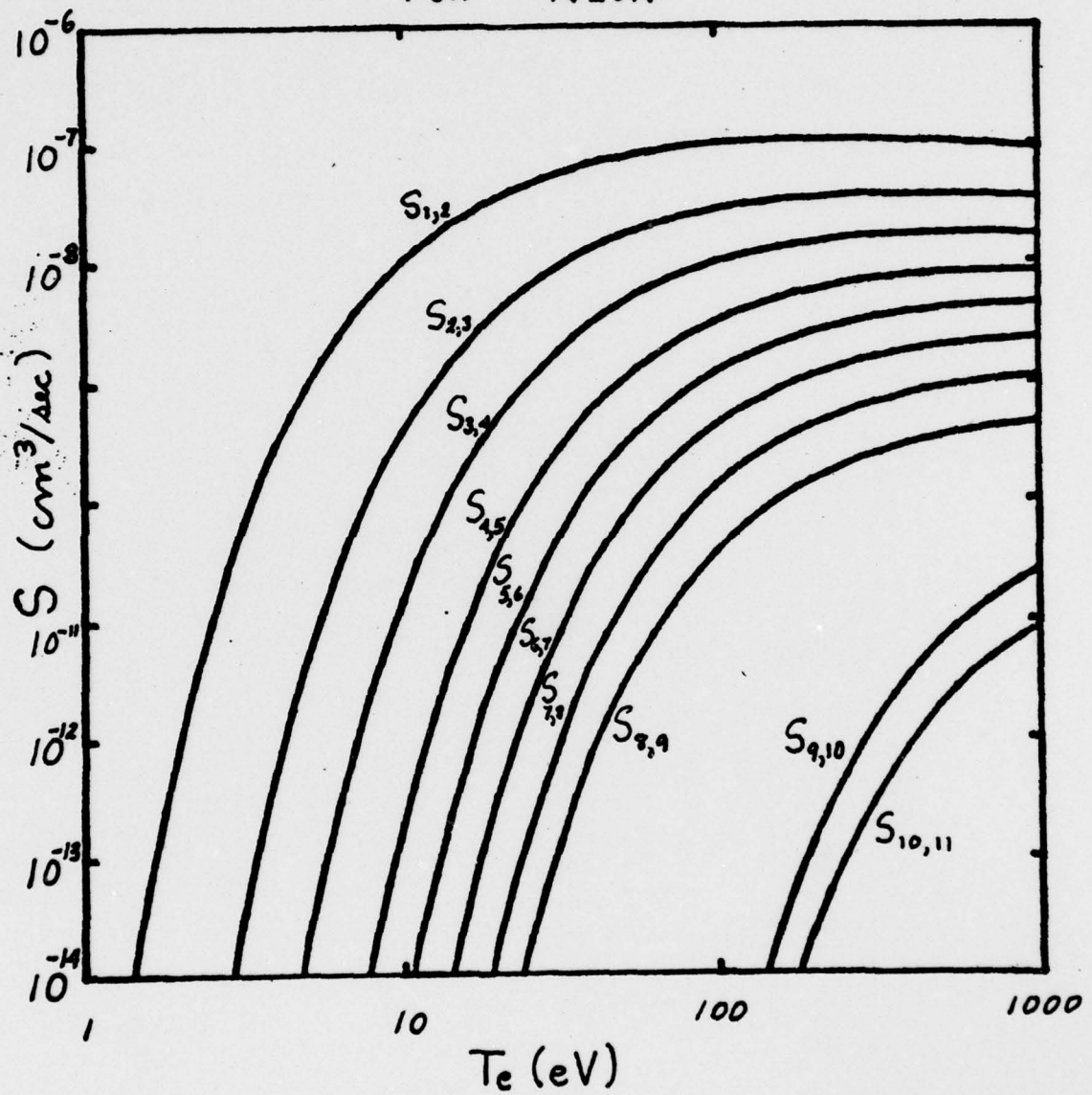
IONIZATION RATE COEFFICIENTS
FOR NEON

Figure 5.3.3

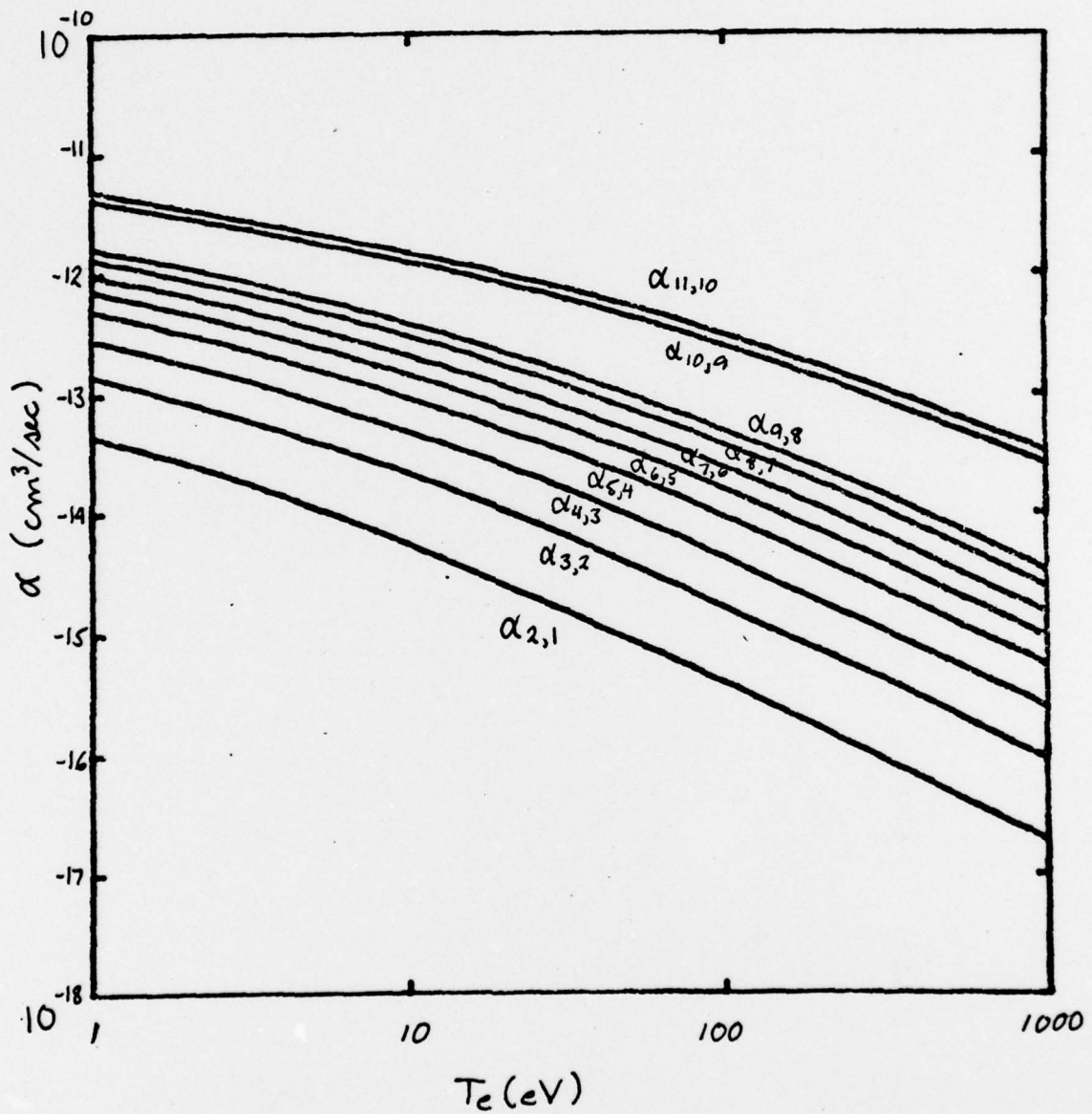
RECOMBINATION RATE COEFFICIENTS
FOR NEON

Figure 5.3.4

greater than that of the sum of the excited states, and Equation 5.2.2 becomes

$$n_j^o Q_j^{o,k} n_e = n_j^k \sum_i A_j^{k,i} \quad (5.4.1)$$

Including the effect of collisional deexcitations, which were not considered in Equation 5.2.2, would only serve to make this approximation more correct.

5.5 Relating Emissivity to Ionic Species Density

The quantity determined from the experiment (Sec. 4.2) is the photon emissivity at the wavelength observed, expressed as $n_j^k A_j^{k,l}$ since it results from the deexcitation of a particular excited state along a particular transition. Since this is a measured quantity, Equation 5.4.1 can be solved for the ion density

by

$$n_j \approx n_j^o = \frac{(n_j^k A_j^{k,l}) \sum_i A_j^{k,i}}{Q_j^{o,k} n_e A_j^{k,l}} \quad (5.5.1)$$

For the resonance transitions in which only one deexcitation transition is possible, Equation 5.5.1 becomes

$$n_j \approx \frac{(n_j^k A_j^{k,l})}{Q_j^{o,k} n_e} \quad (5.5.2)$$

5.6 The Twelfth Species: Ortho-Ne VII

The "notable exception" mentioned in Sec. 5.4 of excited ions returning immediately to the ground state is a form of Ne VII, which will be called ortho-Ne VII, from the parallel which can be

drawn to the same phenomenon observed in helium¹⁷). Ne VII is six times ionized, leaving four electrons in bound shells. Of these, two are tightly bound to the 1S shell and can be disregarded. The ground state of the ion has the remaining two electrons filling the 2S shell, and will be called para-Ne VII. However, if the two outer electrons have the same spin, they are forbidden to both occupy the 2S shell by the exclusion principle. Ortho-Ne VII is probably formed during ionization of Ne VI when the ejected electron is one which leaves the remaining four with an inequality of spin. Examination of Figure 3.1.1 shows that the only strong nonresonance line is that of ortho-Ne VII, at 559 Å, which is the transition from the triplet $2p^2$ state to the triplet 2s2p state. Since the ratio of ortho-Ne VII to para-Ne VII should not be dependent on electron density and temperature, one need only determine this ratio and the density distribution of para-Ne VII to determine the total density distribution of Ne VII.

5.7 Determination of the Ratio of Ortho-Ne VII to Para-Ne VII

There are six transitions of ortho-Ne VII from the triplet $2p^2$ configuration to the triplet 2s2p, which is the "ground state" for ortho-Ne VII. Two of these transitions are grouped near 651 Å, two near 563 Å, and two near 559 Å. The two near 559 Å were the best for observation (since they did not fall near transition lines of other ions), and both fell simultaneously within the 3 Å

resolution of the monochrometer. The fraction of ortho-Ne VII radiating at 559 Å is the sum of the oscillator strengths of the 559 Å pair divided by the sum of all oscillator strengths for the $2p^2-2s2p$ transition, since all other factors in the formula for excitation rates¹² remain the same. The peak brightnesses, looking across the plasma center, were compared for the 559 Å ortho-Ne VII transitions and the 465 Å para-Ne VII resonance transition, after subtracting the no-neon background taken at the same settings in each case. Correcting for the four unobserved transitions of ortho-Ne VII, for the difference in instrument efficiency at the two wavelengths, and for the difference in the excitation rates of the two transitions, the ratio of ortho-Ne VII to para-Ne VII was determined to be 3.17.

5.8 The Absolute Density Distributions of Ne VII and Ne VIII

Neon VII and VIII were the only species bright enough to be observed with good spatial resolution. Application of Equation 5.5.2 and inclusion of the ratio of Sec. 5.7 yields the density distributions for these two ions shown in Figure 5.8.1. The electron density and temperature distributions used in these calculations were based on Spitzer resistivity, Langmuir probe, and 8 mm microwave interferometric measurements¹⁸ and on oxygen evolution studies in Versator I.¹⁹

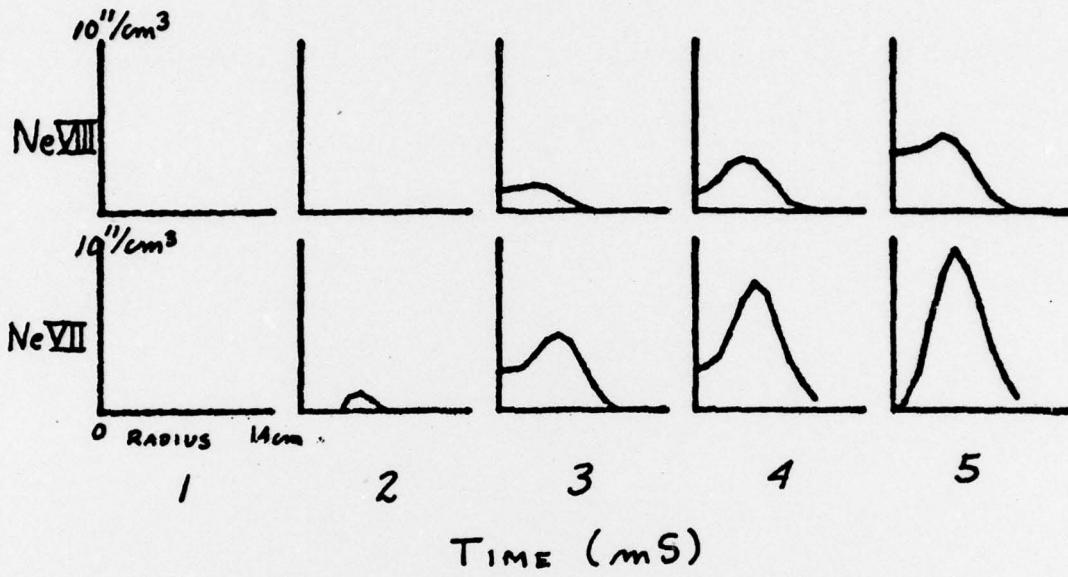


Figure 5.8.1 Absolute Densities of Ne VII and Ne VIII

CHAPTER VI DRIFT VELOCITIES AND CONCLUSIONS

6.1 Approximations to the Corona Equations

The ratio of the ionization rate coefficients to those of recombination is primarily a function of electron temperature,²⁰ and is shown in Figure 6.1.1. From this, it can be seen that at Versator I temperatures the recombination coefficients are at least two orders of magnitude smaller than those for ionization for the Ne VIII to Ne IX pair, and for all lesser ionized states. For the Ne IX to Ne X and the Ne X to Ne XI pairs, recombination rates are two orders of magnitude greater than those of ionization, so that essentially no Ne X or Ne XI is present. The corona equations 5.2.1 can therefore be written

$$\begin{aligned} \frac{dn_j}{dt} &= S_{j-1,j} n_{j-1} n_e - S_{j,j+1} n_j n_e & j = 1,7 \\ \frac{dn_8}{dt} &= S_{7,8} n_7 n_e - S_{8,9} n_8 n_e + \alpha_{9,8} n_9 n_e \\ \frac{dn_9}{dt} &= S_{8,9} n_8 n_e - \alpha_{9,8} n_9 n_e \end{aligned} \quad (6.1.1)$$

The $\alpha_{9,8} n_9 n_e$ term has not been dropped since, although $\alpha_{9,8}$ is much smaller than $S_{8,9}$, Ne IX is the "terminal" species and its density may be much greater than that of Ne VIII. The density of Ne IX can be estimated by neglecting its flow (since Ne IX, presumed to be formed primarily in the more central regions of the plasma, has not much radius over which to flow inwardly). Then,

RATIO OF IONIZATION TO RECOMBINATION
FOR NEON

$$(S_{j,j+1} / \alpha_{j+1,j})$$

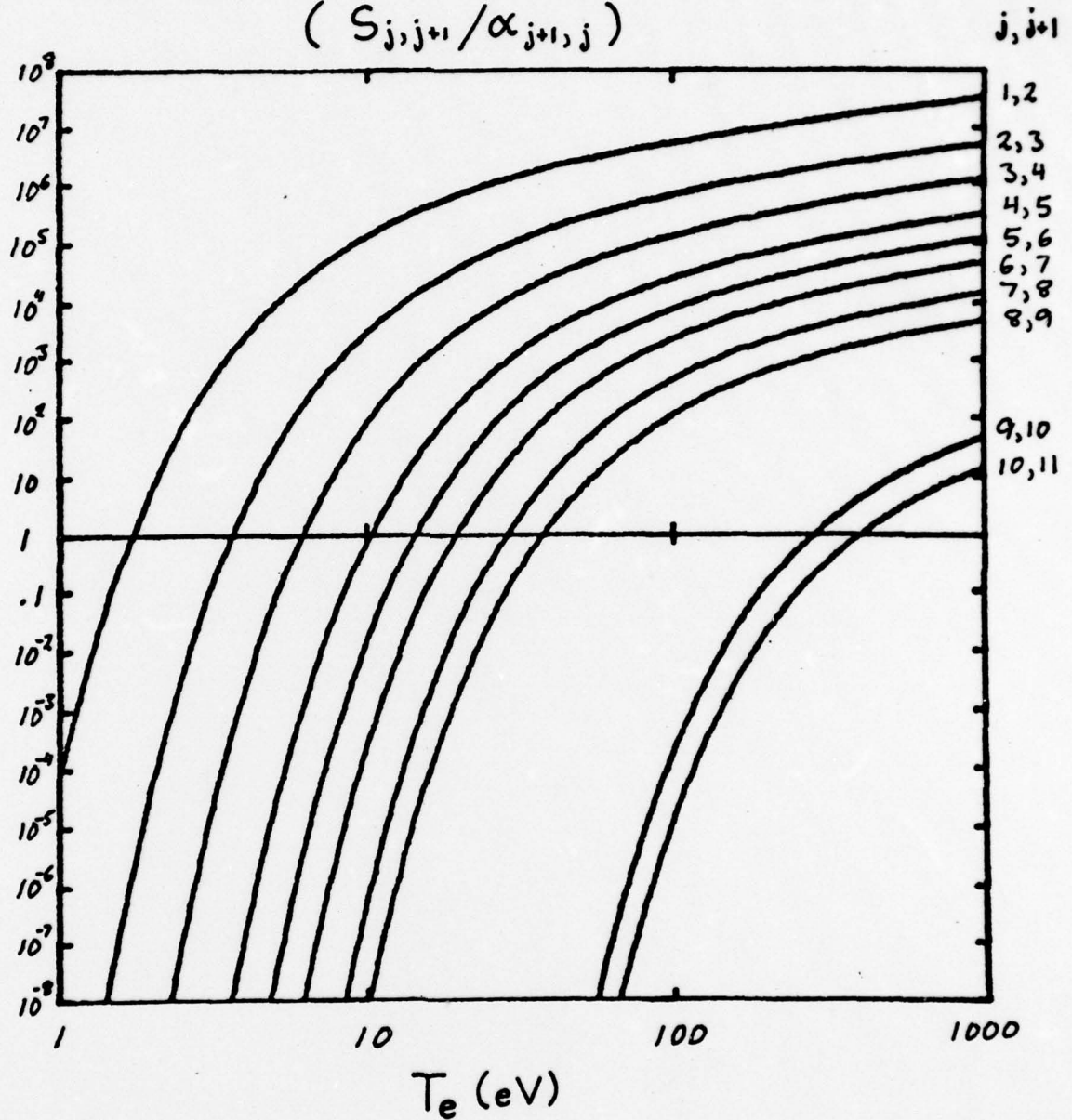


Figure 6.1.1

$$\frac{dn_9}{dt} \approx \frac{\partial n_9}{\partial t} \quad \text{and} \quad n_9(t) \approx \int_0^t (S_{8,9}n_8 - \alpha_{9,8}n_9)n_e dt \quad (6.1.2)$$

Integrating 6.1.2 numerically yields a maximum density for Ne IX (occurring at 5 mS) of $4 \times 10^{10}/\text{cm}^3$. The effect of flows would probably increase this number somewhat, but not enough to make the $\alpha_{9,8}n_e$ product on the order of the $S_{8,9}n_8$ product ($S_{8,9}/\alpha_{9,8} \approx 100$ and $n_9/n_8 \approx 2$). Therefore one can be justified in writing, for times less than 5 mS,

$$\frac{dn_8}{dt} \approx (S_{7,8}n_7 - S_{8,9}n_8)n_e \quad (6.1.3)$$

6.2 Drift Velocities

In radially symmetric cylindrical geometry, Equation 6.1.3 takes the form

$$\frac{\partial n_8}{\partial t} + \frac{1}{r} \frac{\partial}{\partial r}(rn_8 V_8) = (S_{7,8}n_7 - S_{8,9}n_8)n_e \quad (6.2.1)$$

All quantities in this equation are known, except for the drift velocity, V_8 . In principle, a complete description of the transport of neon as a tracer impurity can be formed in this way. However, because the drift velocity term appears in differential form, the values which one obtains for it are sensitive to small errors in all of the other terms.

In order to avoid compounding such errors by integrating (6.2.1) from the wall (where n_8 is zero) or from the center

(where V_g is zero), one can solve for the drift velocity by assuming V_g to be constant over a small interval. After determining the drift velocity distribution in this way, one then checks to see if this assumption is indeed valid.

Using this method, assuming V_g constant over the interval of 2 cm, the results shown in Figure 6.2.1 are obtained. The dotted lines indicate the area over which the assumption of constant V_g is certainly not true. Anomalously, it appears that the Ne VIII is drifting both from the center and from the walls to a radius of about 5 cm, with velocities on the order of 10^4 cm/sec. It cannot be determined whether this is in fact true or is a result of the influence of experimental inaccuracies. Since the same general profile occurs using two different sets of data (those for n_7 and n_8 at 2,3 and 4 mS; and those for n_7 and n_8 at 3,4, and 5 mS) it appears that this apparent drift to an intermediate radius may be the actual case.

6.3 Future Considerations

In future experiments, the use of a grazing incidence monochrometer could make the observation of the Ne IX possible. This observation could answer the question of whether the depression in the Ne VIII density near the plasma center (Figure 4.2.1) is accounted for by Ne IX, or is a phenomenon of impurities not tending to reside in the plasma center.

DRIFT VELOCITIES OF Ne VII

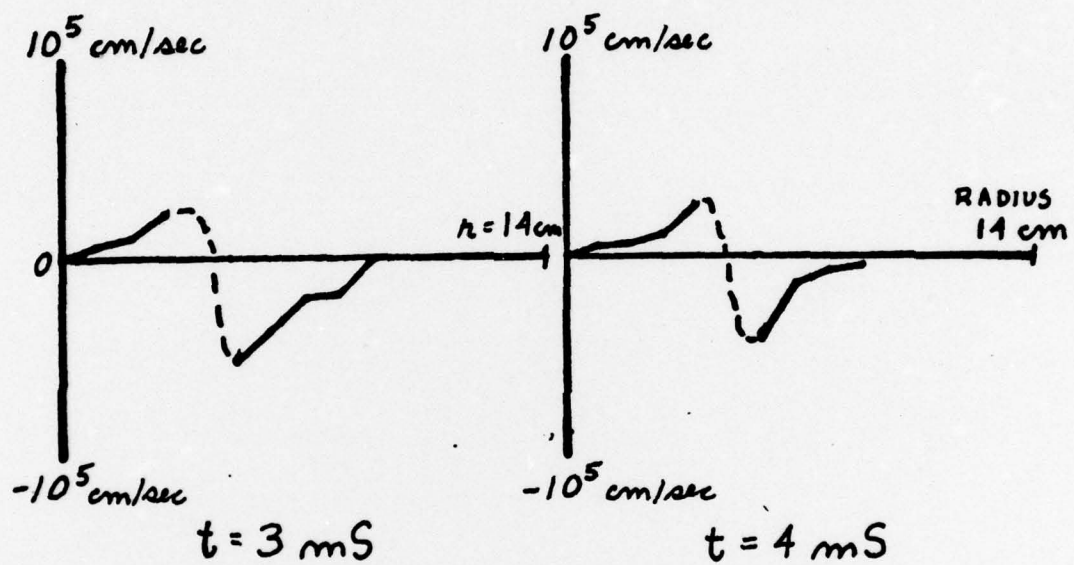


Figure 6.2.1

A device such as Versator II would allow two perpendicular spatial arrays to be made, eliminating the need for the assumption of radial symmetry. With longer plasma durations, steady state conditions would decouple the eleven equations 5.2.1, and permit direct determination of temperature profiles by the ratio of densities.

A device to release the tracer impurity on a time scale short compared to the pulse time would provide a much more useful source function, possibly enabling the determination of a diffusion coefficient.

Neon should be used, if possible, as a tracer since its rate coefficients have recently been experimentally determined, whereas little experimental measurement has been done on the other elements.²¹

Use of the new experimental rates for excitation, ionization, and recombination might correct possibly large errors in the n_7 , n_8 , $S_{7,8}$, and $S_{8,9}$ functions used in Eqn 6.2.1 to determine V_8 .

By determining the density distributions of all impurities in a tokamak plasma, the Z_{eff} as a function of radius and time could be determined.

REFERENCES

- 1 Equipe TFR, Nucl. Fusion 15, 1053 (1975).
- 2 Equipe TFR, EUR-CEA-FC-796 (Nov. 1975).
- 3 S. A. Cohen, J. L. Cecci, and E. S. Marmor, Phys. Rev. Lett. 35, 1507 (1975).
- 4 P. H. Rutherford, Phys. Fluids 17, 1893 (1974).
- 5 Equipe TFR, EUR-CEA-FC-783 (Aug. 1975).
- 6 W. L. Wiese, M. W. Smith, and B. M. Glennon, Atomic Transition Probabilities - Hydrogen Through Neon (NSRDS-NBS4, 1966), Vol. 1.
- 7 W. Lotz, J. Opt. Soc. Am. 58, 915 (1967).
- 8 H. R. Griem, Plasma Spectroscopy, McGraw Hill (1964).
- 9 J. A. R. Samson, Vacuum Ultraviolet Spectroscopy, Wiley & Sons, (1967).
- 10 W. L. Barr, J. Opt. Soc. Am. 52, 885 (1962).
- 11 T. F. Stratton in Plasma Diagnostic Techniques, ed. Huddleston and Leonard (1965).
- 12 H. Van Regemorter, Astrophys. J. 136, 906 (1962).
- 13 W. Lotz, Zeitung Physik 216, 241 (1968).
- 14 W. Lotz, J. Opt. Soc. Am. 58, 915 (1967).
- 15 E. Hinnov, MATT-777 (1970).
- 16 F. K. Richtmeyer, E. H. Kennard, and J. N. Cooper, Introduction to Modern Physics, McGraw Hill (1955).
- 17 D. L. Livesay, Atomic and Nuclear Physics, Blaisdell Pub. (1966).
- 18 D. S. Stone and B. Richards, M. I. T., Cambridge MA, private communication.

REFERENCES (Cont.)

- 19 J. L. Terry, The Johns Hopkins University, Baltimore MD, private communication.
- 20 R. W. P. McWhirter in Plasma Diagnostic Techniques, ed. Huddlestone and Leonard (1965).
- 21 W. L. Wiese, National Bureau of Standards, Wash DC, from an address to the APS on April 27, 1977.

BIOGRAPHICAL NOTE

George Lasche' was born in Fort Leavenworth, Kansas, on July 19, 1947. The son of an Army colonel, he attended thirteen schools until his graduation from high school in Highland Falls, NY, in 1965; and lived in Wash. DC, France, Virginia, Kansas, Pennsylvania, Viet-Nam, Florida, North Carolina, Korea, and New York.

He declined his National Merit Scholarship to accept an appointment to the United States Military Academy at West Point, NY, from which he graduated with a BS and was commissioned a Second Lieutenant in the US Army Corps of Engineers.

After attending the Army Airborne and Ranger schools in Georgia, he was a platoon leader in an engineer construction battalion in Ulm, Germany; a Facilities Engineer in Frankfurt, Germany; and then commanded an engineer construction company of 180 men in Baumholder, Germany, for eighteen months. He then attended the Army Engineer School in Virginia. While there, he gained his license as a Registered Professional Engineer. After serving as a Contracting Officer for the US Government in Korea for a year, he attended MIT for two years. He graduated in June, 1977, with a SM in Physics and a SM in Nuclear Engineering.

Now a captain on active duty, he is assigned to the staff and faculty of West Point as an instructor of Physics.